

Banner appropriate to article type will appear here in typeset article

Excitation and stability of nonlinear compressible Görtler vortices and streaks induced by free-stream vortical disturbances

Dongdong Xu, Pierre Ricco[†], Elena Marensi

School of Mechanical, Aerospace and Civil Engineering, The University of Sheffield, Sheffield, S1 3JD,
United Kingdom

(Received xx; revised xx; accepted xx)

Accepted for publication in *J. Fluid Mech.* (2024).

We study the generation, nonlinear development and secondary instability of unsteady Görtler vortices and streaks in compressible boundary layers exposed to free-stream vortical disturbances and evolving over concave, flat and convex walls. The formation and evolution of the disturbances are governed by the compressible nonlinear boundary-region equations, supplemented by initial and boundary conditions that characterise the impact of the free-stream disturbances on the boundary layer. Computations are performed for parameters typical of flows over high-pressure turbine blades, where the Görtler number, a measure of the curvature effects, and the disturbance Reynolds number, a measure of the nonlinear effects, are order-one quantities. At moderate intensities of the free-stream disturbances, increasing the Görtler number renders the boundary layer more unstable, while increasing the Mach number or the frequency stabilises the flow. As the free-stream disturbances become more intense, vortices over concave surfaces no longer develop into the characteristic mushroom-shaped structures, while the flow over convex surfaces is destabilised. An occurrence map identifies Görtler vortices or streaks for different levels of free-stream disturbances and Görtler numbers. Our calculations capture well the experimental measurements of the enhanced skin friction and wall-heat transfer over turbine-blade pressure surfaces. The time-averaged wall-heat transfer modulations, termed hot fingers, are elongated in the streamwise direction and their spanwise wavelength is half of the characteristic wavelength of the free-stream disturbances. Nonlinearly saturated disturbances are unstable to secondary high-frequency modes, whose growth rate increases with the Görtler number. A new varicose even mode is reported, which may promote transition to turbulence at the stem of nonlinear streaks.

Key words: boundary layer receptivity, instability, transition to turbulence

1. Introduction

Görtler instability originates in boundary layers over concave walls from an inviscid imbalance between pressure and centrifugal forces. The resulting boundary-layer disturbances

[†] Email address for correspondence: p.ricco@sheffield.ac.uk

are steady or low-frequency streamwise-elongated structures – known as Görtler vortices – which play a primary role in driving the laminar-to-turbulence transition in a wide range of industrial and technological applications. In high-speed flows, Görtler vortices are a major concern for the design of hypersonic vehicles, atmospheric re-entry capsules and jet engines, where the intensified wall-shear stresses and wall-heat transfer caused by these vortices pose a severe risk for surface thermal protection (Schneider 1999; Sun & Smith 2017). Görtler vortices are also critical for the design of nozzles in high-speed wind tunnels because they rapidly promote transition to turbulence, which radiates aerodynamic noise that often prevents accurate measurements in the test section and, more seriously, renders the test condition drastically different from that of flight (Beckwith *et al.* 1973; Schneider 2008, 2015).

Of particular interest in our study is the influence of compressible Görtler vortices on the efficiency of turbomachinery, such as high-pressure turbines, characterised by highly curved blade profiles and high levels of ambient disturbances. Despite the ubiquity of Görtler vortices in turbomachinery flows, we note that the literature on Görtler vortices does not often mention turbomachinery applications. At the same time, most studies on turbine blades recognise the presence of disturbed transitional flows, but only a few have paid attention to Görtler vortices. A clear conceptual link between studies on Görtler vortices and turbomachinery flows is therefore missing, although effort and progress to connect the two have been made by Wu, Zhao & Luo (2011) and Xu, Zhang & Wu (2017). Furthermore, one of the key challenges in understanding transitional boundary layers populated by Görtler vortices is their extreme sensitivity to external disturbances, such as free-stream turbulence, whose intensity in turbomachinery flows can reach 20%. The strong influence of external disturbances on Görtler instability needs to be accounted for via a receptivity formalism (Wu *et al.* 2011; Xu *et al.* 2017; Marensi & Ricco 2017).

In this work, we develop a rigorous mathematical and numerical framework to investigate the generation, nonlinear evolution and secondary stability of compressible Görtler vortices excited by free-stream vortical disturbances (FVD) for a range of parameters that are relevant to high-pressure turbine blades. We also study nonlinear compressible streaks evolving over flat surfaces, often called Klebanoff modes (Ricco & Wu 2007; Marensi, Ricco & Wu 2017), and elongated streaky structures appearing over convex surfaces. Receptivity to external vortical disturbances is central in our analysis as it allows linking our work to studies on turbomachinery flows. In §1.1, we summarise theoretical studies of compressible Görtler vortices, including linear stability theory, initial-value theory and initial-boundary-value receptivity theory. Comprehensive reviews of incompressible Görtler instability were given by Hall (1990), Floryan (1991) and Saric (1994). A recent review on theoretical, numerical and experimental studies of compressible Görtler vortices can be found in Xu, Ricco & Duan (2024). Flows over the pressure side of turbine blades are discussed in §1.2. Further details on the scope of our study are given in §1.3.

1.1. Theoretical studies of compressible Görtler vortices

Early studies on incompressible and compressible Görtler vortices neglected the spatial evolution of boundary layers and resorted to a local eigenmode approach by adopting the parallel mean-flow assumption. However, due to the growing nature of free-stream boundary-layer flows, in general, Görtler instability has to be formulated as an initial-value problem, as first rigorously demonstrated in the incompressible case by Hall (1983). Hall (1983) realised that the non-parallel-flow terms cannot be neglected or included in an approximate manner in the study of Görtler instability in the case of order-one Görtler number and characteristic wavelength comparable to the boundary-layer thickness. The non-parallel-flow terms in the equations of motion are of leading order because the streamwise length scale of Görtler

vortices is comparable to that of the base flow. Hall (1983) also showed that the asymptotic limit of large Reynolds number renders the Navier-Stokes equations parabolic along the streamwise direction, i.e. the streamwise diffusion and the streamwise pressure gradient of the perturbations are negligible because they are asymptotically small. The parabolised equations are nowadays called the boundary-region equations (Leib, Wundrow & Goldstein 1999), although this terminology was not used by Hall (1983). The spanwise diffusion is retained because the spanwise wavelength of the disturbance is comparable to the boundary-layer thickness. It should be noted that the initial-boundary-value formulation of Leib *et al.* (1999) is the only theory that takes the external-disturbance receptivity into account. The eigenvalue-problem formulation becomes tenable only when the Görtler number is asymptotically large (Hall 1982).

Hall & Malik (1989) and Hall & Fu (1989) studied compressible Görtler vortices with a wavelength smaller than the boundary-layer thickness under the assumptions of order-one and large Mach numbers, respectively. They concluded that compressibility has a stabilising effect on Görtler instability. A major difference between Görtler vortices in incompressible and compressible flows is the presence of the temperature adjustment layer in the hypersonic limit of large Mach number (Hall & Fu 1989). This layer is located at the edge of the boundary layer, where the temperature of the base flow changes rapidly to its free-stream value. In the limits of large Mach number and large Görtler number, Hall & Fu (1989) analysed Görtler vortices trapped in the adjustment layer by using an eigenvalue approach. The adjustment-layer mode grew the most and therefore the adjustment layer was deemed to be the most dangerous site for secondary instability (Fu & Hall 1991*a*). Dando & Seddougui (1993) and Ren & Fu (2014) studied the competition between the adjustment-layer mode and the conventional wall-layer mode and showed that the former becomes dominant in the hypersonic regime, but it is overtaken by the wall-layer mode for sufficiently large Görtler numbers.

The nonlinear interaction of disturbances in a boundary layer generates harmonics and a mean-flow distortion. Nonlinearity saturates the Görtler vortices when they acquire a significant amplitude. Fu & Hall (1991*b*) first studied the nonlinear development of Görtler vortices in the large Mach-number limit. Bogolepov (2001) investigated the nonlinear evolution of long-wavelength Görtler vortices in hypersonic boundary layers and showed the effects of wall temperature. The eigensolutions of the linear stability problem were used by Ren & Fu (2015) to initiate the downstream computation of the nonlinear parabolised stability equations (this mathematical framework differs from the boundary-region approach, as amply discussed in Xu *et al.* (2024)). It should be noted that the use of eigenfunctions as initial conditions is a common *ad hoc* practice and is only justified when the Görtler number is large. Mushroom-shaped structures of the streamwise velocity, common in flows dominated by Görtler vortices, were found to be replaced by bell-shaped structures during the initial flow evolution. Ren & Fu (2015) ascribed this result to the dominance of the adjustment-layer mode.

Viaro & Ricco (2018, 2019*b,a*) extended the receptivity theory of incompressible Görtler vortices by Wu *et al.* (2011) to the compressible regime and studied the neutral curves of Görtler instability excited by weak FVD. They tackled the receptivity problem by solving the linear compressible boundary-region equations complemented by initial and boundary conditions that synthesise the influence of physically realizable FVD. As opposed to the parabolised stability equations, where the streamwise diffusion and streamwise pressure-gradient terms are modelled by an *ad hoc* numerical procedure, the boundary-region equations are parabolic to leading-order accuracy as they are the rigorous asymptotic limit of the Navier-Stokes equations for low-frequency and long-wavelength perturbations, to which the boundary layer is most receptive.

Marensi *et al.* (2017) solved the nonlinear boundary-region equations to extend the work of Ricco & Wu (2007) on linear compressible streaks to take into account nonlinear effects. Sescu *et al.* (2020) focused on the nonlinear evolution of steady Görtler vortices excited by FVD and computed the wall-shear stress and the wall-heat transfer for Mach numbers varying from 0.8 to 6.

1.2. Flows over high-pressure turbine blades

High-pressure turbine blades are subject to extreme inlet conditions, including high levels of temperature, pressure and unsteadiness of the oncoming turbulence, rendering these flows extremely difficult to measure experimentally and to simulate numerically (Mayle 1991; Zhao & Sandberg 2020). Additional difficulties arise from the strong blade curvature and the effects of wall temperature and pressure gradients. Due to these complexities, most experiments and simulations have been conducted in incompressible flow conditions (Radomsky & Thole 2002; Varty & Ames 2016; Morata *et al.* 2012; Kanani *et al.* 2019; Đurović *et al.* 2021; Lengani *et al.* 2022). Arts, Lambertderouvoit & Rutherford (1990) carried out unique experimental measurements in a compressible wind tunnel and reported data of quantities at the wall. Further boundary-layer measurements, such as those by Radomsky & Thole (2002), are still needed for realistic turbomachinery flow conditions. In a few studies, compressible-flow simulations have been performed (Bhaskaran & Lele 2010; Wheeler *et al.* 2016; Zhao & Sandberg 2020), but a systematic parameter study has not been carried out due to computational limitations.

According to Gourdain, Gicquel & Collado (2012), streamwise vortices are excited in boundary layers over the pressure and suction surfaces of turbine blades. These vortices impact the wall-shear stress and the wall-heat transfer, but their prediction is challenging due to the multitude of factors mentioned earlier. In particular, the influence of the blade curvature on the excitation and evolution of the induced vortices remains obscure. Previous studies have suggested that centrifugal forces could trigger vortices on the pressure surface, as evidenced by the detection of typical Görtler-vortex structures, such as mushrooms and wall ‘hot fingers’ (elongated regions of high wall-heat transfer), as reported by Gourdain *et al.* (2012) and Baughn *et al.* (1995), respectively. However, recent direct numerical simulations have revealed that the concave curvature of the blade is not the sole cause of these vortices, as they also appear in the leading-edge region of both suction and pressure surfaces (Wheeler *et al.* 2016; Zhao & Sandberg 2020). Furthermore, the effect of curvature was not detected in simulations and experiments with elevated free-stream turbulence levels as Görtler vortices with the typical mushroom-shaped structure were not observed (Wheeler *et al.* 2016; Zhao & Sandberg 2020; Arts *et al.* 1990). Đurović *et al.* (2021) numerically identified the appearance of longitudinal vortical structures on the pressure side of low-pressure turbine blades, but ruled out the possibility that these structures were produced by Görtler instability. In their incompressible receptivity study, Xu *et al.* (2017) found that, under high-intensity FVD, Görtler vortices took on the character of streaks, also known as Klebanoff modes, disturbances typically observed in boundary-layer flows over flat plates (Ricco & Wu 2007; Marensi *et al.* 2017).

Despite these research endeavours, a full characterisation of the nature of these structures – Görtler vortices or streaks – in the compressible regime is unavailable. Most importantly, previous incompressible studies, such as those mentioned earlier, can neither predict the temperature field in the boundary layer nor capture typical compressible-flow structures, such as the hot fingers. Understanding the formation of these structures is crucial as it informs the design of cooling techniques to protect the blade surface (Wright *et al.* 2014).

1.3. Scope of our study

Our objective is to study the receptivity, nonlinear evolution and secondary instability of FVD-induced Görtler vortices and streaks in compressible boundary layers. A direct application of our investigation is the dynamics of boundary layers that are typically observed over the pressure and suction surfaces of high-pressure turbines. Our study is based on the earlier investigations of Marensi *et al.* (2017) and Viaro & Ricco (2019a) and it can be viewed as an extension of the former to include centrifugal effects and a generalisation of the latter to the nonlinear case (the reader is referred to table 2 of Xu *et al.* (2024) for an overview of boundary-region receptivity studies). The present work is also an extension of Xu *et al.* (2017) to the compressible regime. The flow parameters are chosen as representative of common turbomachinery flows, in particular with reference to the unique compressible experiments of Arts *et al.* (1990).

We focus on unsteady disturbances because they are likely to be present in boundary layers exposed to high free-stream turbulence environments, such as those over turbine blades (Schultz & Volino 2003). A systematic investigation of the effects of Mach number, wall curvature and FVD intensity on the nonlinear development of Görtler vortices has been carried out, thus uncovering the intricate interplay between these factors in realistic turbomachinery conditions. The unexplained absence of Görtler vortices in flows over turbine blades is elucidated by studying the competition between wall curvature and FVD intensity, thus providing a novel link between Görtler vortices and turbomachinery flow systems. Comparisons with experimental measurements are also presented, showing the key role of the mean-flow distortion in the nonlinear generation of hot fingers over pressure surfaces. Finally, a secondary-instability analysis of the nonlinearly saturated disturbances has revealed the occurrence of a new varicose mode, never reported in previous studies, which may promote transition to turbulence at the stem of streaks.

A limitation of our fundamental analysis is the absence of a pressure gradient, which may impact the flows on both surfaces of a turbine blade and, in particular, induce boundary-layer separation over the suction surface (Nagarajan, Lele & Ferziger 2007). Furthermore, leading-edge bluntness, also absent in the present work, can influence the receptivity of the base flow and the evolution of boundary-layer disturbances through the induced streamwise pressure gradient and by distorting the flow around the stagnation point (Xu *et al.* 2020; Nagarajan *et al.* 2007). Inclusion of these effects in our future work is discussed in the concluding remarks (§5).

2. Mathematical framework

We consider compressible boundary layers flowing over concave, flat and convex surfaces. The radius of curvature of the surface is denoted by r_0^* . Hereafter, the superscript $*$ indicates dimensional quantities. Figure 1 shows a schematic of the flow domain in the concave-wall case. The oncoming base flow is uniform with free-stream velocity U_∞^* and temperature T_∞^* , superimposed on which are unsteady free-stream disturbances. Although free-stream turbulence is of broadband nature, as in Marensi *et al.* (2017) we consider the simplified case of FVD consisting of a pair of vortical modes with the same frequency (and hence streamwise wavenumber), but opposite spanwise wavenumbers $\pm k_z^*$. As streamwise-elongated vortices in a boundary layer typically exhibit a well-defined spanwise spacing Λ^* , it is reasonable to study vortices that are excited by a pair of dominant oblique FVD components.

The flow is described in an orthogonal curvilinear coordinate system, $\mathbf{x}^* = \{x^*, y^*, z^*\}$, that defines the streamwise, wall-normal and spanwise directions. The conversion from the Cartesian to the curvilinear coordinate system is achieved through the Lamé coefficients

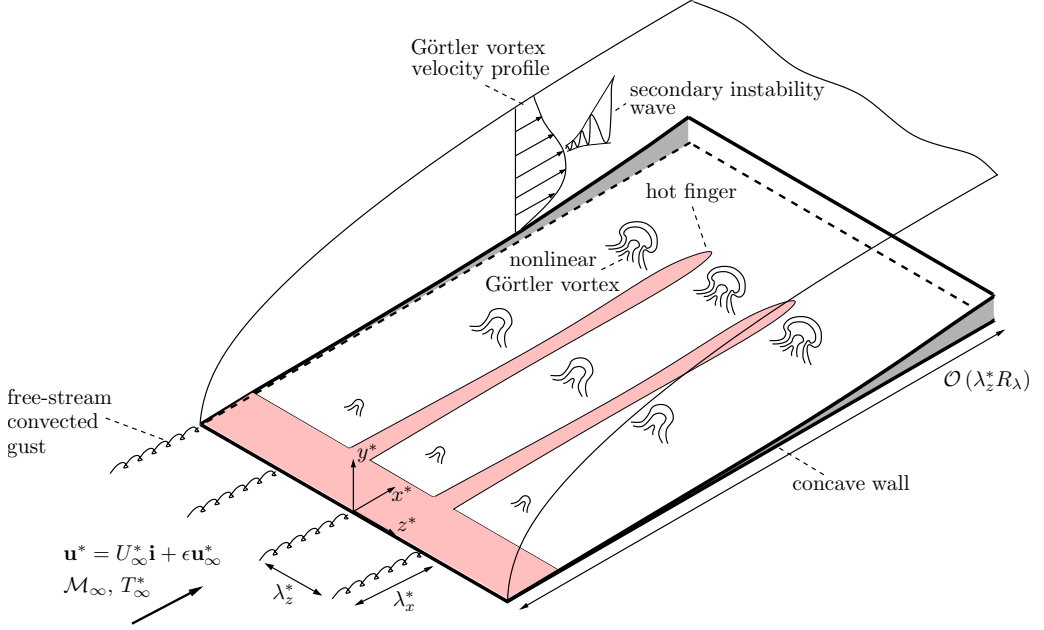


Figure 1: Schematic of the physical domain for the concave-wall case. The sketches of the Görtler vortices and the hot fingers are simply illustrative and do not represent their actual relative positions. The dynamics between the Görtler vortices and the hot fingers is discussed in §4.3.

227 $\{h_x, h_y, h_z\} = \{(r_0^* - y^*)/r_0^*, 1, 1\}$ (Wu *et al.* 2011; Viaro & Ricco 2019a). Lengths are nor-
 228 malised using the length scale $\Lambda^* = 1/k_z^*$, while U_∞^* and T_∞^* are the velocity and temperature
 229 scales. The fluid properties, such as the density ρ^* , the dynamic viscosity μ^* and the thermal
 230 conductivity κ^* , are scaled by their respective constant free-stream values, ρ_∞^* , μ_∞^* and κ_∞^* .
 231 The time t^* and the pressure p^* are non-dimensionalised by Λ^*/U_∞^* and $\rho_\infty^* U_\infty^{*2}$, respectively.
 232 The free-stream disturbance \mathbf{u}_∞ is expressed as

$$233 \quad \mathbf{u} - \mathbf{i} = \epsilon \mathbf{u}_\infty(x - t, y, z) = \epsilon \left(\hat{\mathbf{u}}_+^\infty e^{ik_z z} + \hat{\mathbf{u}}_-^\infty e^{-ik_z z} \right) e^{ik_x(x-t) + ik_y y} + \text{c.c.}, \quad (2.1)$$

234 where $\epsilon \ll 1$ is a measure of the disturbance intensity, \mathbf{i} is the unit vector along the streamwise
 235 direction and c.c. indicates the complex conjugate. The gust disturbance (2.1) is passively
 236 advected by the free-stream base flow, i.e. the phase velocity is U_∞^* because the disturbance is
 237 of small amplitude and specified at small x distances, where viscous effects play a secondary
 238 role, and at large y distances, where the displacement effect induced by the boundary layer
 239 is negligible. The vector $\hat{\mathbf{u}}_\pm^\infty = \{\hat{u}_{x,\pm}^\infty, \hat{u}_{y,\pm}^\infty, \hat{u}_{z,\pm}^\infty\} = O(1)$ satisfies the solenoidal condition

$$240 \quad k_x \hat{u}_{x,\pm}^\infty + k_y \hat{u}_{y,\pm}^\infty \pm k_z \hat{u}_{z,\pm}^\infty = 0. \quad (2.2)$$

241 The Reynolds number R_Λ is defined as

$$242 \quad R_\Lambda = \frac{\rho_\infty^* U_\infty^* \Lambda^*}{\mu_\infty^*} \quad (2.3)$$

243 and is taken to be asymptotically large, i.e. $R_\Lambda \gg 1$. The scaled wavenumbers $\kappa_y =$
 244 $k_y / \sqrt{k_x R_\Lambda} = O(1)$ and $\kappa_z = k_z / \sqrt{k_x R_\Lambda} = O(1)$ are also defined. To account for centrifugal

effects, a Görtler number is introduced,

$$\mathcal{G} = \frac{R_\Lambda^{1/2} \Lambda^*}{k_x^{3/2} r_0^*} = O(1). \quad (2.4)$$

In the present study only unsteady disturbances ($k_x \neq 0$) are considered and therefore the Görtler number is well defined. The Görtler number G_Λ defined in Viaro & Ricco (2019a) is related to \mathcal{G} by $\mathcal{G} = (\kappa_z/k_z)^3 G_\Lambda$. Note that $\mathcal{G} = O(1)$ only if $\kappa_z = O(1)$, which is the case in the present analysis. As a measure of nonlinear effects, we introduce the disturbance Reynolds number $r_t = \epsilon R_\Lambda = O(1)$, as in Leib *et al.* (1999) and Ricco *et al.* (2011). The oncoming flow is isentropic and air is assumed to be a perfect gas. The free-stream Mach number is defined as $M_\infty = U_\infty^*/a_\infty^* = O(1)$, where $a_\infty^* = (\gamma R^* T_\infty^*)^{1/2}$ is the speed of sound in the free stream, $R^* = 287.06 \text{ J kg}^{-1} \text{ K}^{-1}$ is the ideal gas constant for air and $\gamma = 1.4$ is the ratio of the specific heat capacities.

We focus on low-frequency, long-streamwise-wavelength free-stream disturbances ($k_x \ll 1$) because boundary layers are most receptive to these perturbations. Experimental evidence has shown that low-frequency disturbances are those that amplify the most inside wall-bounded shear layers (Matsubara & Alfredsson 2001). The plate is thin and the Mach number is moderate so that shocks are assumed to be weak and distant from the boundary layer. The effects of shocks on the free-stream perturbations and the boundary layer are therefore neglected. The reader is referred to Qin & Wu (2016) for the response of a flat-plate hypersonic boundary layer to free-stream acoustic, vortical and entropy disturbances downstream of a shock.

The flow domain is divided into four asymptotic regions, described in Viaro & Ricco (2019a). The region of interest is region III, where the spanwise and wall-normal viscous effects are comparable and the streamwise coordinate is scaled with the streamwise wavenumber of the free-stream disturbance, i.e. $\bar{x} = k_x x = O(1)$. The distinguished relationship $k_x = O(R_\Lambda^{-1})$ emerges from the asymptotic balance and the slow time variable $\bar{t} = k_x t = O(1)$ is defined. The streamwise velocity is larger than the wall-normal and spanwise velocities by a factor $O(R_\Lambda)$ and larger than the pressure by a factor $O(R_\Lambda^2)$. The velocity, pressure and temperature variables are rescaled as

$$\{u^*, v^*, w^*\} / U_\infty^* = \{\tilde{u}, \sqrt{k_x / R_\Lambda} \tilde{v}, k_x \tilde{w}\}, \quad p^* / (\rho_\infty^* U_\infty^{*2}) = k_x R_\Lambda^{-1} \tilde{p}, \quad T^* / T_\infty^* = \tilde{T}. \quad (2.5)$$

By substituting expression (2.5) into the compressible Navier-Stokes equations written in curvilinear coordinates and by performing the change of variable $(x, t) \rightarrow (\bar{x}, \bar{t})$, we obtain the following leading-order nonlinear boundary-region equations:

$$\frac{\partial \tilde{p}}{\partial \bar{t}} + \frac{\partial \tilde{p} \tilde{u}}{\partial \bar{x}} + \frac{\kappa_z}{k_z} \frac{\partial \tilde{p} \tilde{v}}{\partial y} + \frac{\partial \tilde{p} \tilde{w}}{\partial z} = 0, \quad (2.6)$$

$$\tilde{\rho} \frac{\partial \tilde{u}}{\partial \bar{t}} + \tilde{\rho} \tilde{u} \frac{\partial \tilde{u}}{\partial \bar{x}} + \tilde{\rho} \tilde{v} \frac{\kappa_z}{k_z} \frac{\partial \tilde{u}}{\partial y} + \tilde{\rho} \tilde{w} \frac{\partial \tilde{u}}{\partial z} = \frac{\kappa_z^2}{k_z^2} \left[\frac{\partial}{\partial y} \left(\tilde{\mu} \frac{\partial \tilde{u}}{\partial y} \right) + \frac{\partial}{\partial z} \left(\tilde{\mu} \frac{\partial \tilde{u}}{\partial z} \right) \right], \quad (2.7)$$

$$\begin{aligned} & \tilde{\rho} \frac{\partial \tilde{v}}{\partial \bar{t}} + \tilde{\rho} \tilde{u} \frac{\partial \tilde{v}}{\partial \bar{x}} + \tilde{\rho} \tilde{v} \frac{\kappa_z}{k_z} \frac{\partial \tilde{v}}{\partial y} + \tilde{\rho} \tilde{w} \frac{\partial \tilde{v}}{\partial z} + \mathcal{G} \tilde{u}^2 = \\ & \frac{\kappa_z}{k_z} \left\{ -\frac{\partial \tilde{p}}{\partial y} + \frac{\partial}{\partial y} \left[\frac{2}{3} \tilde{\mu} \left(\frac{2\kappa_z}{k_z} \frac{\partial \tilde{v}}{\partial y} - \frac{\partial \tilde{w}}{\partial z} \right) \right] + \frac{\partial}{\partial z} \left[\tilde{\mu} \left(\frac{\kappa_z}{k_z} \frac{\partial \tilde{v}}{\partial z} + \frac{\partial \tilde{w}}{\partial y} \right) \right] - \frac{\partial}{\partial y} \left(\frac{2}{3} \tilde{\mu} \frac{\partial \tilde{u}}{\partial \bar{x}} \right) + \frac{\partial}{\partial \bar{x}} \left(\tilde{\mu} \frac{\partial \tilde{u}}{\partial y} \right) \right\}, \end{aligned} \quad (2.8)$$

$$\begin{aligned} & \tilde{\rho} \frac{\partial \tilde{w}}{\partial \tilde{t}} + \tilde{\rho} \tilde{u} \frac{\partial \tilde{w}}{\partial \tilde{x}} + \tilde{\rho} \tilde{v} \frac{\kappa_z}{k_z} \frac{\partial \tilde{w}}{\partial y} + \tilde{\rho} \tilde{w} \frac{\partial \tilde{w}}{\partial z} = \\ & \frac{\kappa_z^2}{k_z^2} \left\{ -\frac{\partial \tilde{p}}{\partial z} + \frac{\partial}{\partial z} \left[\frac{2}{3} \tilde{\mu} \left(2 \frac{\partial \tilde{w}}{\partial z} - \frac{\kappa_z}{k_z} \frac{\partial \tilde{v}}{\partial y} \right) \right] + \frac{\partial}{\partial y} \left[\tilde{\mu} \left(\frac{\kappa_z}{k_z} \frac{\partial \tilde{v}}{\partial z} + \frac{\partial \tilde{w}}{\partial y} \right) \right] - \frac{\partial}{\partial z} \left(\frac{2}{3} \tilde{\mu} \frac{\partial \tilde{u}}{\partial \tilde{x}} \right) + \frac{\partial}{\partial \tilde{x}} \left(\tilde{\mu} \frac{\partial \tilde{u}}{\partial z} \right) \right\}, \end{aligned} \quad (2.9)$$

$$\begin{aligned} & \tilde{\rho} \frac{\partial \tilde{T}}{\partial \tilde{t}} + \tilde{\rho} \tilde{u} \frac{\partial \tilde{T}}{\partial \tilde{x}} + \tilde{\rho} \tilde{v} \frac{\kappa_z}{k_z} \frac{\partial \tilde{T}}{\partial y} + \tilde{\rho} \tilde{w} \frac{\partial \tilde{T}}{\partial z} = \\ & \frac{\kappa_z^2}{k_z^2} \left\{ \frac{1}{Pr} \left[\frac{\partial}{\partial y} \left(\tilde{\mu} \frac{\partial \tilde{T}}{\partial y} \right) + \frac{\partial}{\partial z} \left(\tilde{\mu} \frac{\partial \tilde{T}}{\partial z} \right) \right] + (\gamma - 1) \mathcal{M}_\infty^2 \tilde{\mu} \left[\left(\frac{\partial \tilde{u}}{\partial y} \right)^2 + \left(\frac{\partial \tilde{u}}{\partial z} \right)^2 \right] \right\}. \end{aligned} \quad (2.10)$$

The flow is decomposed as the sum of the compressible Blasius flow and the perturbation flow induced by the FVD, namely

$$\{\tilde{u}, \tilde{v}, \tilde{w}, \tilde{p}, \tilde{T}\} = \left\{ U, V, 0, \frac{1}{\gamma \mathcal{M}_\infty}, T \right\} + r_t \{\bar{u}, \bar{v}, \bar{w}, \bar{p}, \bar{\tau}\}(\bar{x}, \eta, z, \bar{t}), \quad (2.11)$$

where $\{U, V\} = \{F'(\eta), T(\eta_c F' - F)/\sqrt{2\bar{x}}\}$, $T = T(\eta)$,

$$\eta = \sqrt{\frac{R_\Lambda}{2x}} \int_0^y \rho(\bar{x}, \bar{y}) d\bar{y}, \quad \eta_c = \frac{1}{T} \int_0^\eta T(\tilde{\eta}) d\tilde{\eta}, \quad (2.12)$$

and $\rho = T^{-1}$. The prime denotes differentiation with respect to the similarity variable η . The compressible Blasius functions $F(\eta)$ and $T(\eta)$ are solutions to the boundary-value problem,

$$\left. \begin{aligned} & (\mu F''/T)' + FF'' = 0, \\ & (\mu T'/T)' + Pr FT' + \mu(\gamma - 1) Pr \mathcal{M}_\infty^2 (F'')^2/T = 0, \\ & F = F' = 0, \quad T = T_w, \quad \text{at } \eta = 0, \\ & F' \rightarrow 1, \quad T' = 0, \quad \text{as } \eta \rightarrow \infty, \end{aligned} \right\} \quad (2.13)$$

where the Prandtl number Pr is assumed constant, $Pr = 0.707$, the dynamic viscosity is $\mu(T) = T^\omega$ with $\omega = 0.76$ (Stewartson 1964) and the thermal conductivity is $\kappa = \mu$. Curvature effects are negligible at leading order in system (2.13) because of the assumptions $R_\Lambda \gg 1$ and $r_0 \gg 1$ (Hall 1983).

The density is decomposed as $\tilde{\rho} = T^{-1} + r_t \bar{\rho}$, where, using the equation of state for a perfect gas, $\bar{\rho} = -\bar{\tau}/T^2 - r_t \bar{\rho} \bar{\tau}/T + \mathcal{O}(k_x R_\Lambda^{-1})$. The viscosity is expressed as $\tilde{\mu} = (T + r_t \tau)^\omega$ and expanded using the binomial formula as in equation (2.21) of Marensi *et al.* (2017).

The boundary-layer disturbance consists of all temporal and spanwise harmonics

$$\begin{aligned} \{\bar{u}, \bar{v}, \bar{w}, \bar{p}, \bar{\tau}\} = & \sum_{m,n=-\infty}^{\infty} \left\{ \hat{u}_{m,n}(\bar{x}, \eta), \sqrt{2\bar{x}} \hat{v}_{m,n}(\bar{x}, \eta), k_z^{-1} \hat{w}_{m,n}(\bar{x}, \eta), \right. \\ & \left. \hat{p}_{m,n}(\bar{x}, \eta), \hat{\tau}_{m,n}(\bar{x}, \eta) \right\} e^{im\bar{t} + ink_z z}. \end{aligned} \quad (2.14)$$

As the physical quantities are real, the Fourier coefficients are Hermitian, $\hat{q}_{-m,-n} = (\hat{q}_{m,n})_{cc}$, where \hat{q} stands for any of $\{\hat{u}, \hat{v}, \hat{w}, \hat{p}, \hat{\tau}\}$. Inserting expressions (2.11) and (2.14) into the nonlinear boundary-region equations (2.6)-(2.10) yields the governing equations for the disturbance Fourier coefficients.

311 The continuity equation

$$\begin{aligned}
 312 \quad & \frac{\eta_c}{2\bar{x}} \frac{T'}{T} \hat{u}_{m,n} + \frac{\partial \hat{u}_{m,n}}{\partial \bar{x}} - \frac{\eta_c}{2\bar{x}} \frac{\partial \hat{u}_{m,n}}{\partial \eta} - \frac{T'}{T^2} \hat{v}_{m,n} + \frac{1}{T} \frac{\partial \hat{v}_{m,n}}{\partial \eta} + i n \hat{w}_{m,n} \\
 313 \quad & - \left(\frac{i m}{T} + \frac{1}{2\bar{x}} \frac{FT'}{T^2} \right) \hat{\tau}_{m,n} - \frac{F'}{T} \frac{\partial \hat{\tau}_{m,n}}{\partial \bar{x}} + \frac{1}{2\bar{x}} \frac{F}{T} \frac{\partial \hat{\tau}_{m,n}}{\partial \eta} = r_t \hat{C}_{mn}. \quad (2.15)
 \end{aligned}$$

314 The x-momentum equation

$$\begin{aligned}
 315 \quad & \left(i m - \frac{\eta_c}{2\bar{x}} F'' + n^2 \kappa_z^2 \mu T \right) \hat{u}_{m,n} + F' \frac{\partial \hat{u}_{m,n}}{\partial \bar{x}} - \frac{1}{2\bar{x}} \left(F + \frac{\mu' T'}{T} - \frac{\mu T'}{T^2} \right) \frac{\partial \hat{u}_{m,n}}{\partial \eta} \\
 316 \quad & - \frac{1}{2\bar{x}} \frac{\mu}{T} \frac{\partial^2 \hat{u}_{m,n}}{\partial \eta^2} + \frac{F''}{T} \hat{v}_{m,n} + \frac{1}{2\bar{x} T} \left(F F'' - \mu'' F'' T' + \frac{\mu' F'' T'}{T} - \mu' F''' \right) \hat{\tau}_{m,n} \\
 317 \quad & - \frac{1}{2\bar{x}} \frac{\mu' F''}{T} \frac{\partial \hat{\tau}_{m,n}}{\partial \eta} = r_t \hat{X}_{mn}. \quad (2.16)
 \end{aligned}$$

318 The y-momentum equation

$$\begin{aligned}
 319 \quad & \frac{1}{4\bar{x}^2} \left[\eta_c (F T' - F' T) - \eta_c^2 F'' T + F T \right] \hat{u}_{m,n} + \frac{\mu' T'}{3\bar{x}} \frac{\partial \hat{u}_{m,n}}{\partial \bar{x}} - \frac{\mu}{6\bar{x}} \frac{\partial^2 \hat{u}_{m,n}}{\partial \bar{x} \partial \eta} \\
 320 \quad & + \frac{\eta_c \mu}{12\bar{x}^2} \frac{\partial^2 \hat{u}_{m,n}}{\partial \eta^2} + \frac{1}{12\bar{x}^2} \left(\eta_c \mu' T' + \mu - \frac{\eta_c \mu T'}{T} \right) \frac{\partial \hat{u}_{m,n}}{\partial \eta} \\
 321 \quad & + \left[\frac{1}{2\bar{x}} \left(F' + \eta_c F'' - \frac{F T'}{T} \right) + i m + n^2 \kappa_z^2 \mu T \right] \hat{v}_{m,n} \\
 322 \quad & + F' \frac{\partial \hat{v}_{m,n}}{\partial \bar{x}} + \frac{1}{\bar{x}} \left[\frac{2}{3T} \left(\frac{\mu T'}{T} - \mu' T' \right) - \frac{F}{2} \right] \frac{\partial \hat{v}_{m,n}}{\partial \eta} - \frac{2}{3\bar{x}} \frac{\mu}{T} \frac{\partial^2 \hat{v}_{m,n}}{\partial \eta^2} + i n \frac{\mu' T'}{3\bar{x}} \hat{w}_{m,n} \\
 323 \quad & - i n \frac{\mu}{6\bar{x}} \frac{\partial \hat{w}_{m,n}}{\partial \eta} + \frac{1}{2\bar{x}} \frac{\partial \hat{p}_{m,n}}{\partial \eta} \\
 324 \quad & + \left[\frac{1}{3\bar{x}^2 T} \left(\mu'' F T'^2 - \frac{\mu' F T'^2}{T} + \mu' F T'' + \mu' F' T' \right) - \frac{1}{4\bar{x}^2} \left(F' F - \eta_c F'^2 - \eta_c F F'' \right. \right. \\
 325 \quad & \left. \left. + \frac{F^2 T'}{T} + \mu' F'' + \eta_c \mu'' F'' T' - \frac{\eta_c \mu' F'' T'}{T} + \eta_c F''' \mu' \right) \right] \hat{\tau}_{m,n} + \frac{\mu'}{\bar{x}^2} \left(\frac{F T'}{3T} - \frac{\eta_c F''}{4} \right) \frac{\partial \hat{\tau}_{m,n}}{\partial \eta} \\
 326 \quad & - \frac{\mu' F''}{2\bar{x}} \frac{\partial \hat{\tau}_{m,n}}{\partial \bar{x}} + \frac{\mathcal{G}}{\sqrt{2\bar{x}}} \left(2 F' \hat{u}_{m,n} - \frac{F'^2}{T} \hat{\tau}_{m,n} \right) \\
 327 \quad & = r_t \left[\hat{\mathcal{Y}}_{mn} - \frac{\mathcal{G}}{\sqrt{2\bar{x}}} \left(2 F' T \widehat{\rho \bar{u}} + \widehat{\bar{u} \bar{u}} + r_t T \widehat{\rho \bar{u} \bar{u}} \right) - F'^2 \widehat{\rho \bar{\tau}} \right]. \quad (2.17)
 \end{aligned}$$

328 The z-momentum equation

$$\begin{aligned}
 329 \quad & \frac{i n \kappa_z^2 \eta_c \mu' T T'}{2\bar{x}} \hat{u}_{m,n} - \frac{i n \kappa_z^2 \mu T}{3} \frac{\partial \hat{u}_{m,n}}{\partial \bar{x}} + \frac{i n \kappa_z^2 \eta_c \mu T}{6\bar{x}} \frac{\partial \hat{u}_{m,n}}{\partial \eta} - i n \kappa_z^2 \mu' T' \hat{v}_{m,n} - \frac{i n \kappa_z^2 \mu}{3} \frac{\partial \hat{v}_{m,n}}{\partial \eta} \\
 330 \quad & + \left(\frac{4}{3} n^2 \kappa_z^2 \mu T + i m \right) \hat{w}_{m,n} + F' \frac{\partial \hat{w}_{m,n}}{\partial \bar{x}} + \frac{1}{2\bar{x}} \left(\frac{\mu T'}{T^2} - F - \frac{\mu' T'}{T} \right) \frac{\partial \hat{w}_{m,n}}{\partial \eta} - \frac{1}{2\bar{x}} \frac{\mu}{T} \frac{\partial^2 \hat{w}_{m,n}}{\partial \eta^2} \\
 331 \quad & + i n \kappa_z^2 T \hat{p}_{m,n} - \frac{i n \kappa_z^2}{3\bar{x}} \mu' F T' \hat{\tau}_{m,n} = r_t \hat{\mathcal{Z}}_{mn}. \quad (2.18)
 \end{aligned}$$

The energy equation

$$\begin{aligned}
 & -\frac{\eta_c}{2\bar{x}} T' \hat{u}_{m,n} + \frac{T'}{T} \hat{v}_{m,n} + \left[\frac{FT'}{2\bar{x}T} + im + \frac{n^2 \kappa_z^2 \mu T}{Pr} - \frac{1}{2\bar{x}Pr} \left(\frac{\mu' T'}{T} \right)' \right] \hat{t}_{m,n} + F' \frac{\partial \hat{t}_{m,n}}{\partial \bar{x}} \\
 & + \frac{1}{2\bar{x}} \left(\frac{\mu T'}{PrT^2} - F - \frac{2\mu' T'}{PrT} \right) \frac{\partial \hat{t}_{m,n}}{\partial \eta} - \frac{1}{2\bar{x}Pr} \frac{\mu}{T} \frac{\partial^2 \hat{t}_{m,n}}{\partial \eta^2} \\
 & - \mathcal{M}_\infty^2 \frac{\gamma - 1}{\bar{x}T} \left(\mu F'' \frac{\partial \hat{u}_{m,n}}{\partial \eta} + \frac{\mu' F''^2}{2} \hat{t}_{m,n} \right) = r_t \hat{\mathcal{E}}_{mn}.
 \end{aligned} \tag{2.19}$$

where $\mu' = d\mu/dT$ and the nonlinear terms $\hat{\mathcal{C}}_{mn}, \hat{\mathcal{X}}_{mn}, \hat{\mathcal{Y}}_{mn}, \hat{\mathcal{Z}}_{mn}, \hat{\mathcal{E}}_{mn}$ are given in equations (A1)-(A5) of Marensi *et al.* (2017). The nonlinear terms collected on the right-hand sides of equations of (2.15)-(2.19) vanish as $r_t \rightarrow 0$ and the linearised boundary-region equations of Viaro & Ricco (2019a) are recovered.

In the boundary layer, the velocity and temperature fluctuations induced near the leading edge are of small amplitude, and thus evolve linearly in this region. Curvature effects near the leading edge are also negligible and therefore the initial conditions for the forced modes $(m, n) = (1, \pm 1)$ are the same as those in the linear flat-plate case (Ricco & Wu 2007). The initial conditions are given in Appendix A. Matching the boundary-region solution with the outer solution gives the outer boundary conditions

$$\{\hat{u}_{m,n}, \hat{v}_{m,n}, \hat{w}_{m,n}, \hat{p}_{m,n}, \hat{t}_{m,n}\} \rightarrow \left\{ 0, \frac{\kappa_z}{\sqrt{2\bar{x}}} v_{m,n}^\dagger, \kappa_z^2 w_{m,n}^\dagger, \frac{\epsilon}{k_x} p_{m,n}^\dagger, 0 \right\} \text{ as } \eta \rightarrow \infty, \tag{2.20}$$

where $v_{m,n}^\dagger, w_{m,n}^\dagger, p_{m,n}^\dagger$ are given by equations (2.76) in Marensi *et al.* (2017). The initial-boundary-value problem, consisting of equations (2.15)-(2.19), (A1)-(A5) and (2.20), governs the excitation and nonlinear evolution of Görtler vortices in the presence of FVD for $r_t = O(1)$, $\mathcal{G} = O(1)$ and $\mathcal{M}_\infty = O(1)$.

2.1. Secondary instability

The velocity and temperature profiles altered by nonlinearity are sensitive to high-frequency secondary disturbances as they exhibit inflection points in the transverse and spanwise directions during certain phases of the oscillations. These high-frequency secondary disturbances amplify and ultimately cause transition to turbulence in boundary layers over the pressure surface of turbine blades (Butler *et al.* 2001) and in wind-tunnel experiments (Ghorbanian *et al.* 2011). A secondary instability analysis of the boundary-layer flow perturbed by nonlinear disturbances is therefore carried out to elucidate the transition process.

The flow q is decomposed into a base flow $\tilde{q}(y, z; \bar{x}, \bar{t})$, given by (2.11), and a secondary perturbation flow $q'_s(x, y, z, t)$, namely

$$q(y, z; x, t) = \tilde{q} + \epsilon_s q'_s = \tilde{q} + \epsilon_s \{ \rho'_s, u'_s, v'_s, w'_s, T'_s \} (x, y, z, t), \tag{2.21}$$

where $\epsilon_s \ll 1$. Substituting expression (2.21) into the full compressible Navier-Stokes equations and neglecting the $O(\epsilon_s^2)$ nonlinear terms, we obtain the linearised compressible Navier-Stokes equations. Since the base-flow \tilde{u} and \tilde{T} vary slowly with \bar{x} and \bar{t} , the dependence on these two variables can be treated as parametric when the short-wavelength (of order δ^*) and the high-frequency (of order U_∞/δ^*) instability is considered. A solution is sought in the normal-mode form

$$q'_s(x, y, z, t) = q_s(y, z) \exp[i(\alpha x - \omega t)] + \text{c.c.}, \tag{2.22}$$

where α is the streamwise wavenumber and ω is the frequency of the secondary disturbance.

The shape function $q_s(y, z) = \{u_s, v_s, w_s, T_s\}$ is governed by a system of partial differential equations, supplemented by homogeneous boundary conditions, $\{u_s, v_s, w_s, T_s\} = 0$ at $y = 0$ and $\{u_s, v_s, w_s, T_s\} \rightarrow 0$ as $y \rightarrow \infty$.

For a spanwise-periodic base flow \tilde{q} , the solution for q_s can be expressed using Floquet theory as

$$q_s = e^{i\gamma\beta z} \sum_{k=-\infty}^{\infty} \phi_{s,k}(y) e^{ik\beta z}, \quad (2.23)$$

where β is the spanwise wavenumber and $0 \leq \gamma \leq 1/2$. Fundamental modes ($\gamma = 0$), subharmonic modes ($\gamma = 1/2$) and detuned modes ($0 < \gamma < 1/2$) are all part of the same branch of instability modes but with varying spanwise wavelengths. The growth rate of the modes was found to be insensitive to the Floquet parameter (Ren & Fu 2015).

3. Numerical procedures

The initial-boundary-value problem, i.e. the nonlinear boundary-region equations (2.15)-(2.19) supplemented by the initial conditions (A 1)-(A 5) and the outer boundary conditions (2.20), is solved numerically. The boundary-region equations are parabolic in the streamwise direction and therefore can be solved by a marching procedure in the \bar{x} -direction. A second-order backward finite-difference scheme in the \bar{x} -direction and a second-order central finite-difference scheme in the η -direction are employed. In order to avoid the pressure decoupling phenomenon, the pressure is computed on a grid that is staggered in the η -direction with respect to the grid for the velocity components and temperature. The nonlinear terms are evaluated using the pseudo-spectral method. In order to prevent aliasing errors, i.e. the spurious energy cascade from the unresolved high-frequency modes into the resolved low-frequency ones, the 3/2-rule is applied (Canuto *et al.* 1988). The resulting block tri-diagonal system is solved using a standard block-elimination algorithm. A second-order predictor-corrector under-relaxation scheme is used to calculate the nonlinear terms while marching downstream, as in the computation of incompressible Görtler vortices by Xu *et al.* (2017). The use of under-relaxation for capturing the generation of nonlinear streaks was deemed unnecessary by Marensi *et al.* (2017). However, it is needed in our analysis to stabilise the computations, given the high growth rate and intensity exhibited by Görtler vortices. The wall-normal domain extends to $\eta_{max} = 60$ and 2000 grid points are used in this direction. The typical step size in the marching direction is $\Delta\bar{x} = 0.01$. To capture the nonlinear effects, it is sufficient to use $N_t=17$ modes to discretise time and $N_z=17$ modes to discretise the spanwise direction.

The equations governing the secondary instability are discretised using a five-point finite-difference scheme with fourth-order accuracy along the wall-normal direction and Fourier spectral expansion along the spanwise direction. The code was used by Song, Zhao & Huang (2020) to perform a secondary-instability analysis of nonlinear stationary vortices.

4. Results

4.1. Flow parameters

The nonlinear boundary-layer disturbances are studied for parameters that characterise flows over high-pressure turbine blades. The flow parameters chosen as reference are given in table 1. As discussed in Marensi *et al.* (2017), they are inspired by typical experimental works on turbomachinery applications, such as Arts *et al.* (1990) and Camci & Arts (1990). In the figure captions, only the parameters that are varied in the figure are given. In all our

M_∞	T_w	R_Λ	\mathcal{G}	k_x	κ_z	κ_y	Tu	$\epsilon \cdot 10^2$		
0.69	0.75	1124	35.2	0.0073	0.35	0.35	1% 4% 6%	0.35	1.41	2.11

Table 1: Reference flow parameters.

computations, the scaled amplitudes of the free-stream velocity components are $\hat{u}_{x,\pm}^\infty = \hat{u}_{y,\pm}^\infty = 1$ and $\hat{u}_{z,\pm}^\infty = \mp 1$. The continuity relation (2.2) reduces to $k_x + k_y \pm 1 = 0$.

The adiabatic wall temperature is calculated using the relation valid for a perfect gas, $T_{ad} = 1 + (\gamma - 1)\sqrt{Pr}M_\infty^2/2$. The non-dimensional wall temperature is $T_w = 0.75$ as blade cooling is often applied to avoid excessive wall-heat transfer. The axial chord length of the turbine blade is $C_{ax}^* = 0.0388$ m. This length corresponds to the maximum streamwise coordinate $\bar{x} = 0.558$ for $k_x = 7.3 \cdot 10^{-3}$, our chosen frequency representative of the experiments of Arts *et al.* (1990) and Camci & Arts (1990). The reference radius of curvature is $r_0^* = 1.4$ m and the spanwise length scale is $\Lambda^* = 0.89 \cdot 10^{-3}$ m, corresponding to a Görtler number $\mathcal{G} = 35.2$. The FVD level varies between $Tu = 1\%$ and 6% , as in the experiments of Arts *et al.* (1990). For the form of perturbations assumed here, the FVD level Tu is related to the FVD intensity ϵ by $Tu(\%) = 100 \cdot 2\epsilon (\hat{u}_{x,+}^{\infty 2} + \hat{u}_{x,-}^{\infty 2})^{1/2}$.

We investigate the effect of three parameters on the evolution of boundary-layer disturbances, i.e. the Görtler number \mathcal{G} , the FVD level Tu and the Mach number M_∞ . Boundary-layer transition is also affected by the free-stream disturbance length scales (e.g. as recently shown by Fransson & Shahinfar (2020)). The impact of k_x on the evolution of the boundary-layer disturbances was studied in detail in our previous studies (Marensi *et al.* 2017; Xu *et al.* 2017; Marensi & Ricco 2017) and similar effects are expected in the present case. Furthermore, as verified in several experimental campaigns, boundary-layer disturbances have a spanwise length that is comparable to the boundary-layer thickness and therefore we fix $\kappa_z, \kappa_y = \mathcal{O}(1)$.

The overall intensity of the disturbances is measured by the root mean square (r.m.s.) of the fluctuating quantity, defined as

$$q_{rms,max}(\bar{x}) = \max_{\eta} q_{rms}(\bar{x}, \eta) = \max_{\eta} r_t \sqrt{\sum_{m=-N_t}^{N_t} \sum_{n=-N_z}^{N_z} |\hat{q}_{m,n}|^2}, \quad m \neq 0, \quad (4.1)$$

where q stands for any quantity, but we focus on the streamwise velocity and the temperature because they are the leading-order variables.

4.2. Velocity and temperature of the nonlinear boundary-layer disturbances

The effect of Görtler number on the downstream evolution of the streamwise and temperature disturbances is studied first. The variation of Görtler number is achieved by adjusting the boundary-layer curvature while keeping the frequency constant. Figure 2 depicts the downstream development of $u_{rms,max}$ and $\tau_{rms,max}$ for four different Görtler numbers, including the flat-wall case ($\mathcal{G} = 0$) and a convex-wall case ($\mathcal{G} = -281.6$). Two FVD levels are tested ($Tu = 1\%$ and $Tu = 6\%$). The coordinate x_s on top of the graphs is normalised by the axial chord length C_{ax}^* (the end of the turbine blade is at $x_s = 1.65$). For $Tu = 1\%$, the concave wall destabilises the flow, whereas the convex wall has a marked stabilising effect on the growth of both the velocity and temperature disturbances. For $Tu = 6\%$, the curvature has little effect in the concave-wall case and is stabilising in the convex-wall case. The evolutions of the vortical structures for $\mathcal{G} = 35.2$ and $\mathcal{G} = 70.4$ are indeed almost the same as in the

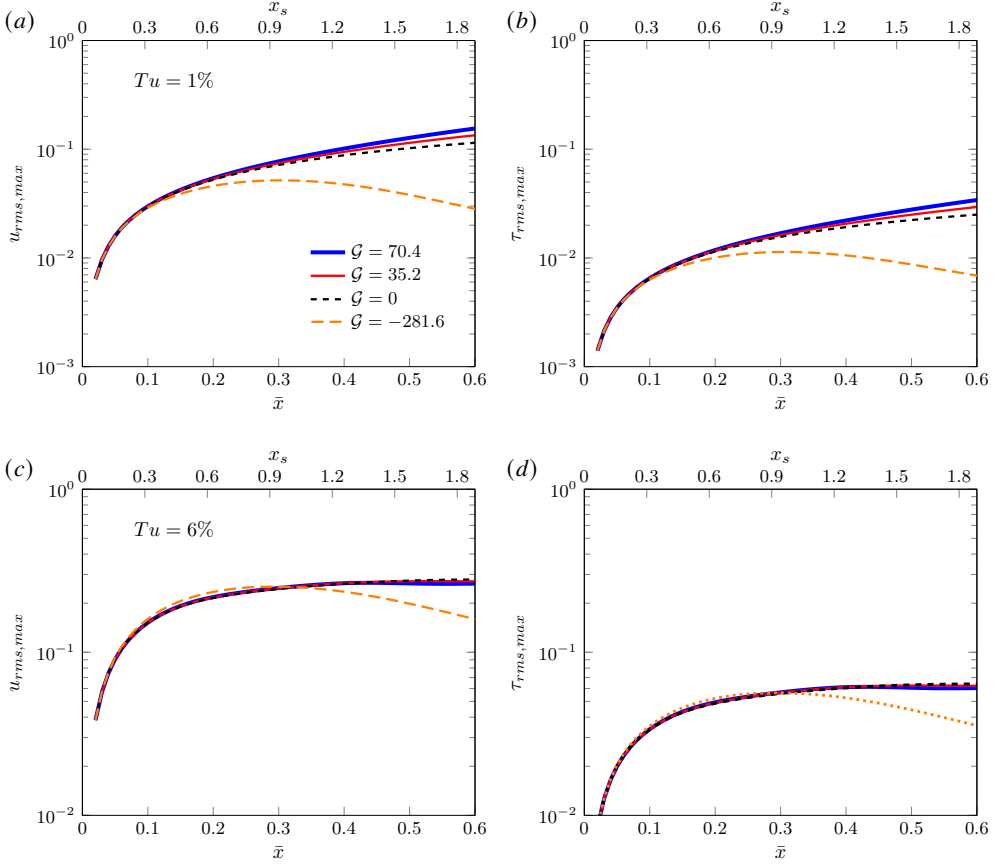


Figure 2: Effect of Görtler number on the downstream development of $u_{rms,max}$ and $\tau_{rms,max}$ induced by (a, b) $Tu = 1\%$ and (c, d) $Tu = 6\%$.

flat-wall case. The convex curvature is not influential up to $\bar{x} = 0.35$ for such a higher FVD level. For the cases considered, the boundary-layer dynamics is therefore largely independent of the curvature up to $x_s = 1.2$, i.e. for most of the extent of the turbine blade.

Figure 3(a, b) shows the effect of the FVD level on the downstream development of $u_{rms,max}$ and $\tau_{rms,max}$ for $\mathcal{G} = 35.2$. For $Tu = 1\%$, Görtler vortices undergo non-modal growth and gradually evolve to nonlinear saturation, similarly to incompressible cases (Xu *et al.* 2017; Marensi & Ricco 2017). For the high-intensity cases, $Tu = 4\%$ and $Tu = 6\%$, the vortices saturate after a much shorter non-modal growth than in the $Tu = 1\%$ case. The values of $u_{rms,max}$ and $\tau_{rms,max}$ saturate to almost the same level for different FVD intensities. This behaviour is different from that of compressible streaks over flat plates, where the perturbation intensity depends significantly on the FVD level (Marensi *et al.* 2017). As shown in figure 3(c, d), the intensity of the disturbances evolving over convex walls is enhanced by increasing the FVD level, similarly to the flat-wall case.

The Mach-number effect on the Görtler vortices is studied by keeping the Reynolds number, the frequency and the radius of curvature constant. The change of Mach number with a constant Reynolds number can be achieved through an adjustment of the total pressure (hence, the density), as in the experiments of Huang, Si & Lee (2021), and by use of the

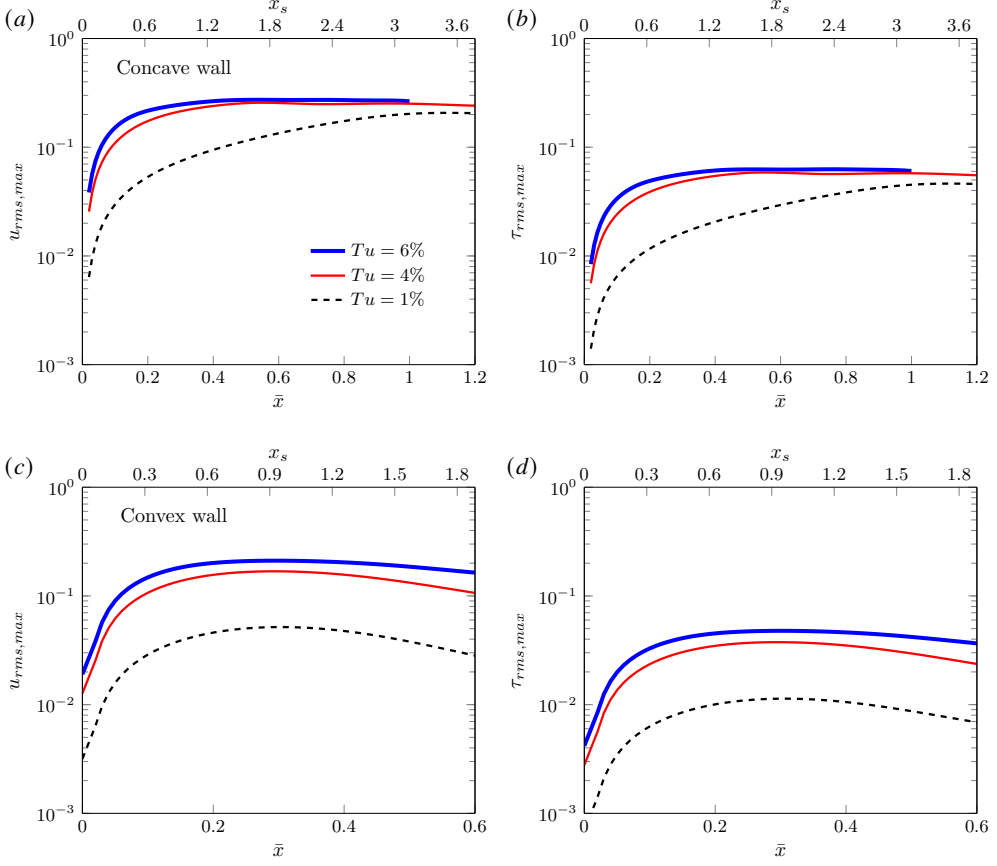


Figure 3: Effect of FVD level on the downstream development of $u_{rms,max}$ and $\tau_{rms,max}$ over (a, b) concave wall ($\mathcal{G} = 35.2$) and (c, d) convex wall ($\mathcal{G} = -281.6$).

relation $R_\Lambda = \mathcal{M}_\infty \rho_\infty^* \Lambda^* / (\sqrt{\gamma R^* T_\infty^*} \mu_\infty^*)$, as discussed in Viaro & Ricco (2019a). Figure 4 shows the effect of Mach number on the evolution of Görtler vortices induced by low-intensity FVD ($Tu = 1\%$) and high-intensity FVD ($Tu = 6\%$). Figure 4(a) illustrates that the growth of the streamwise velocity is not influenced by the Mach number. The growth of the thermal disturbances is instead affected by the Mach number, as shown in figure 4(b). They are slightly stabilised as the Mach number increases within the subsonic range, unaffected in transonic conditions, and moderately enhanced in supersonic conditions.

The Mach-number effect in our cases is markedly different from that reported by Viaro & Ricco (2019a) in their figure 6. Viaro & Ricco (2019a) showed that, as the Mach number increases from the incompressible condition, the r.m.s. of the streamwise velocity is attenuated, while the r.m.s. of the temperature increases for a short distance from the leading edge and decreases further downstream. The difference in dynamics between our flows and those in Viaro & Ricco (2019a) is due to the higher Görtler number and frequency of our cases. As both these quantities become larger, the boundary-layer response becomes less sensitive to a change in Mach number.

Figure 5 shows the development of the maximum amplitudes of the fundamental and the harmonic temperature Fourier modes for $\mathcal{G} = 35.2, 0$ and -281.6 . The Görtler number plays a different role at low ($Tu = 1\%$) and high ($Tu = 6\%$) FVD levels. In all cases, the fundamental

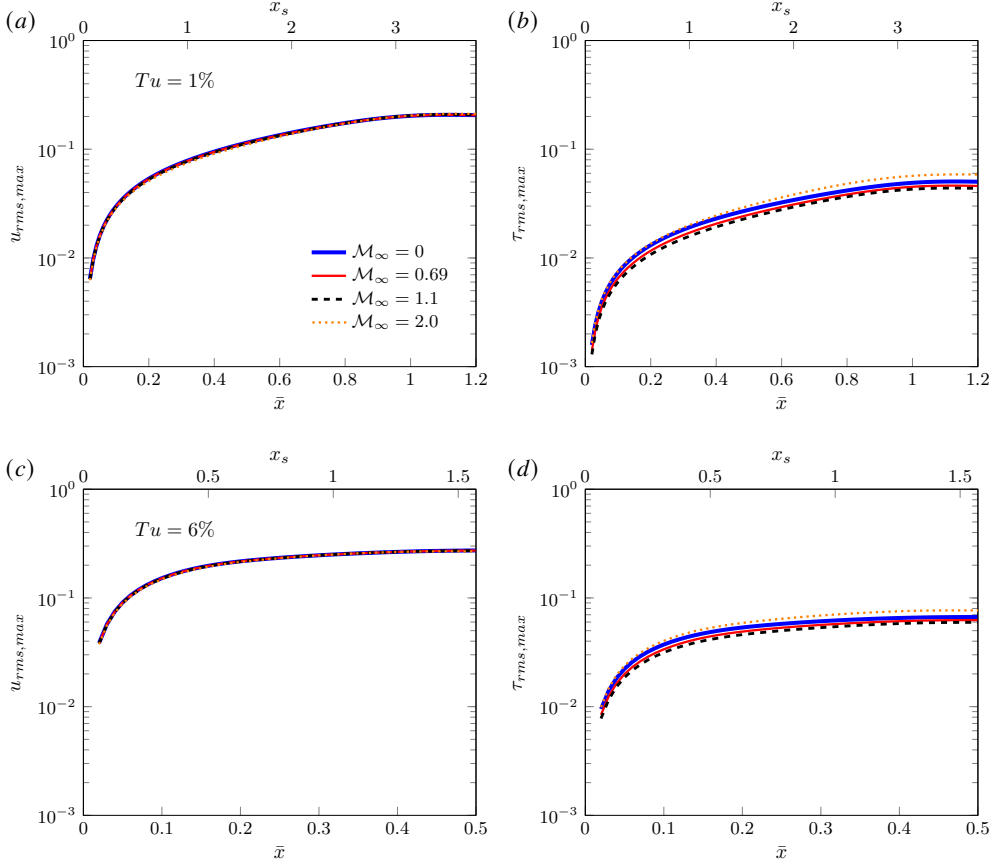


Figure 4: Effect of Mach number on the downstream development of $u_{rms,max}$ and $\tau_{rms,max}$ for (a, b) $Tu = 1\%$ and (c, d) $Tu = 6\%$. The Görtler number is $\mathcal{G} = 35.2$.

modes $(1, \pm 1)$ are initially dominant over all the other modes. For the case with $\mathcal{G} = 35.2$, shown in figures 5(a, b), the mean-flow distortion given by the mode $(0, 0)$ grows significantly downstream, acquiring a magnitude larger than that of the fundamental modes $(1, \pm 1)$. The cross-over streamwise location moves closer to the leading edge as the FVD level increases. The amplitude of the other harmonics remains smaller than that of the fundamental modes $(1, \pm 1)$ at any location. In the flat-wall case for $Tu = 1\%$, shown in figure 5(c), the cross-over of modes $(1, \pm 1)$ and $(0, 0)$ also occurs and all the modes keep growing downstream up to saturation, but their amplitude is lower than that in the concave case. As shown in figure 5(e), for the convex-wall case and $Tu = 1\%$, the fundamental modes $(1, \pm 1)$ are dominant over all the other harmonics and the overtake of the mean-flow distortion does not occur within the streamwise distance studied. Differently from the flat-wall case, all the modes grow and eventually decay in the convex-wall case. Figures 5(d, f) show that, in the flat-wall and convex-wall cases for $Tu = 6\%$, the mode $(0, 0)$ surpasses the fundamental modes $(1, \pm 1)$. For $Tu = 6\%$, the cross-over location moves closer to the leading edge as the Görtler number increases.

Of particular interest are the streamwise velocity and temperature profiles of the perturbed boundary-layer flow. Figure 6 shows the instantaneous profiles at $z = 0$ and different phases $\phi = k_x t$, for three different Görtler numbers. For $\mathcal{G} = 35.2$, the profiles exhibit great variation

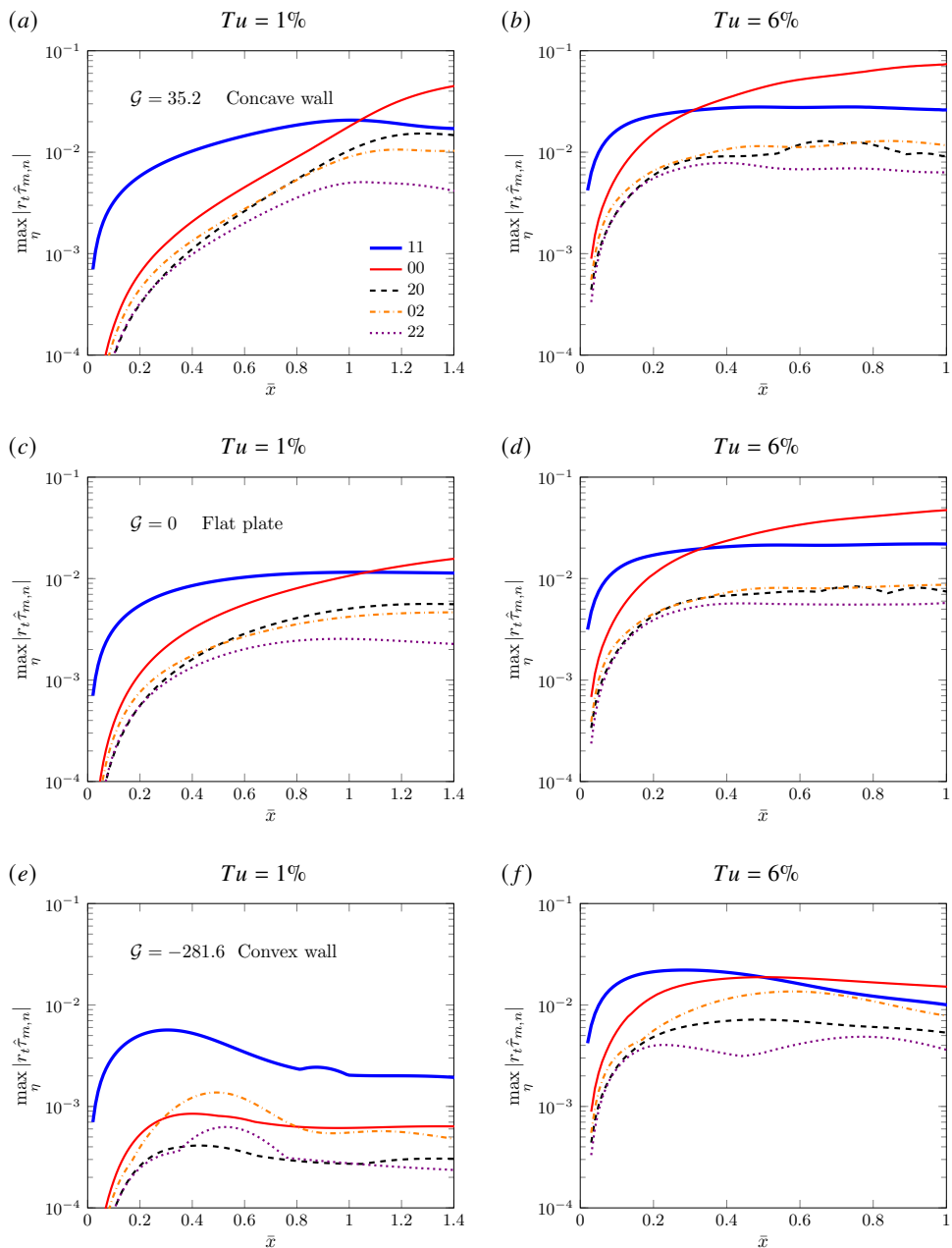


Figure 5: Development of the fundamental mode $(m, n) = (1, 1)$ and the harmonic components $(m, n) = (0, 0)$, $(2, 0)$, $(0, 2)$, $(2, 2)$ of temperature disturbance for different Görtler numbers: (a,b) $\mathcal{G} = 35.2$, (c,d) $\mathcal{G} = 0$, and FVD levels: (a,c,e) $Tu = 1\%$, (b,d,f) $Tu = 6\%$. Only modes with $n \geq 0$ are shown as modes $(m, \pm n)$ have the same amplitude for the free-stream disturbance of the assumed form.

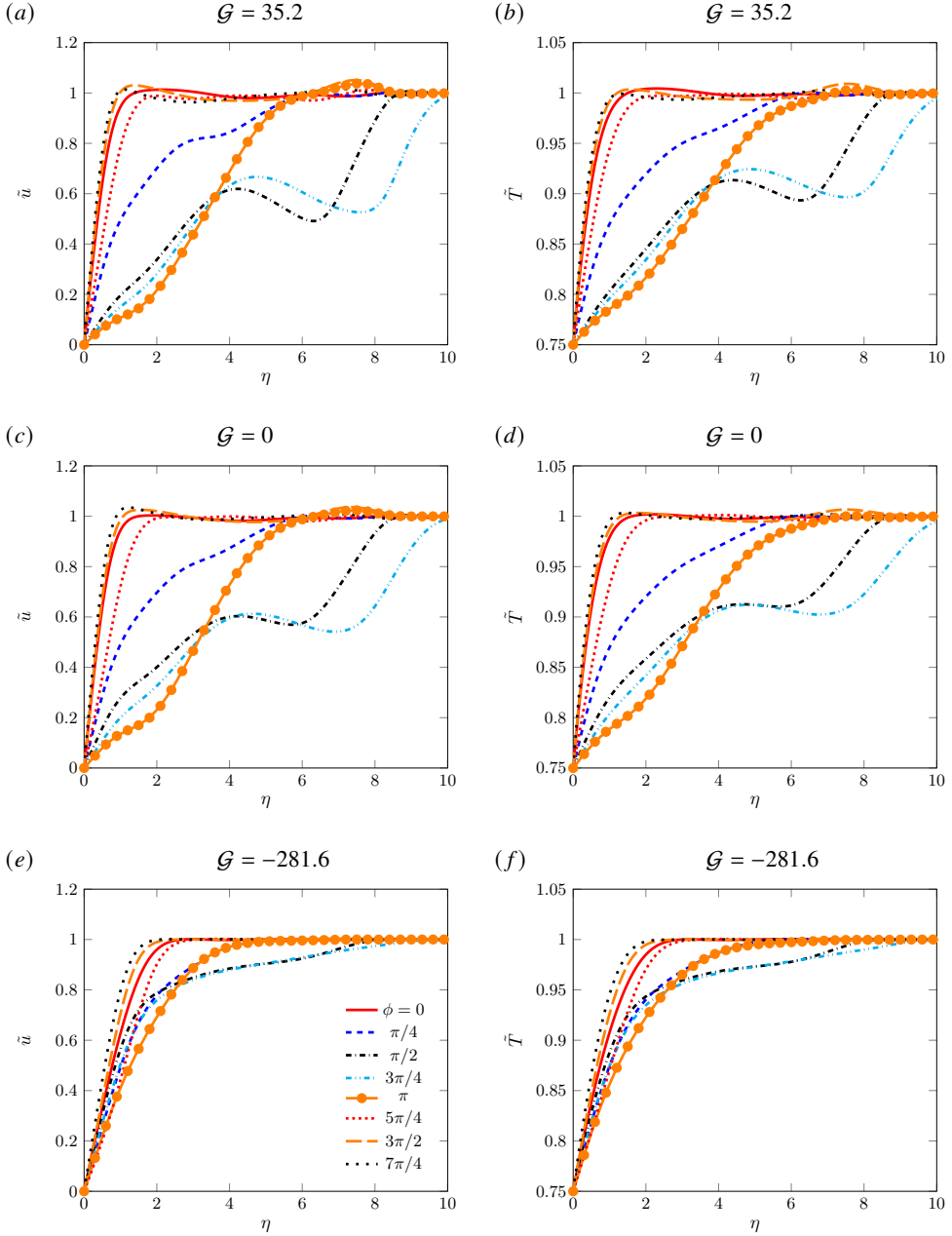


Figure 6: Profiles of instantaneous (a, c, e) streamwise velocity and (b, d, f) temperature at $\bar{x} = 0.54$, $z = 0$ for $Tu = 6\%$ and different Görtler numbers.

with the phase, becoming highly inflectional at certain phases ($\phi = \pi/2$ and $3\pi/4$). This behaviour suggests that the flow may be inviscidly unstable. The variation becomes slightly weaker for the flat-wall case and subsides in the convex-wall case, for which the profiles are much less inflectional.

Contours of the instantaneous \tilde{u} and \tilde{T} in y - z planes are displayed in figure 7 for a moderate

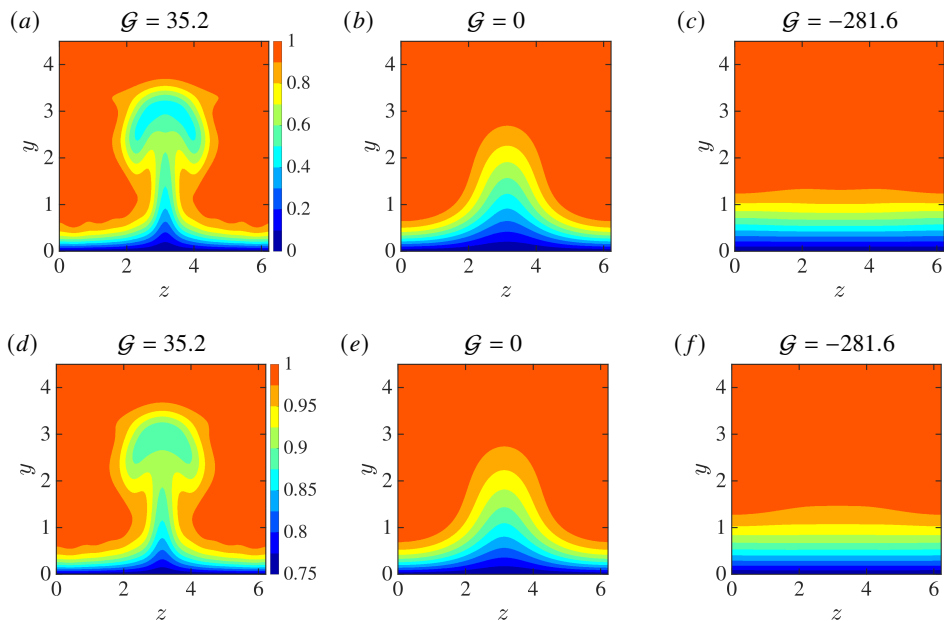


Figure 7: Contours of the instantaneous (a – c) streamwise velocity and (d – f) temperature in the $y - z$ plane for $Tu = 1\%$ at $\bar{x} = 1.5$. The increment of the contour values is 0.1 for the velocity and 0.05 for the temperature. The coordinate y is related to the similarity variable η via $y = \sqrt{2x/R_\Lambda} \int_0^\eta T(\eta) d\eta$.

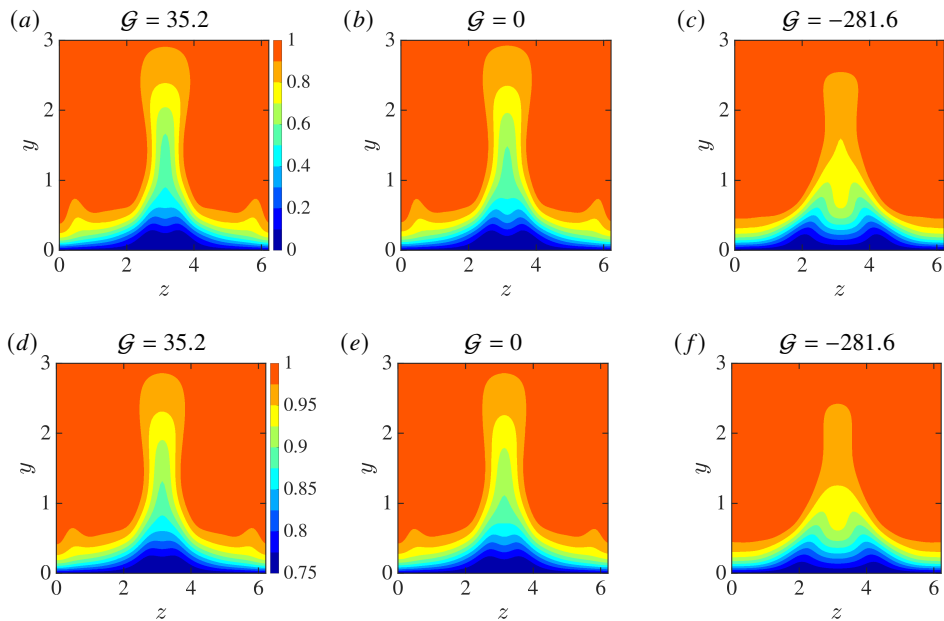


Figure 8: Contours of the instantaneous (a – c) streamwise velocity and (d – f) temperature in the $y - z$ plane for $Tu = 6\%$ at $\bar{x} = 0.36$. The increment of the contour values is 0.1 for the velocity and 0.05 for the temperature.

FVD level ($Tu=1\%$) and in figure 8 for a high FVD level ($Tu=6\%$). The contours are shown at phases where the disturbances obtain maximum amplitude and at sufficiently downstream locations where they have saturated. Figure 7 shows that, for the moderate FVD level $Tu = 1\%$, the velocity and temperature disturbances exhibit the typical mushroom shape in the concave case, while the bell shape, characteristic of streaky structures, appears in the flat-wall case. The flow remains largely undisturbed when the wall is convex.

We note that the mushroom shapes could be observed over a concave plate in a wind tunnel because of the long extent of the test section. However, the downstream locations of figures 7(a) and 7(d) are too large for these structures to be observed in practical turbomachinery applications because of the limited length of turbine blades. As shown by the abscissas at the top of figure 2(a), locations beyond $\bar{x} = 1$ considerably exceed the length of a turbine blade, estimated to be $x_s = 1.65$ by using the flow parameters in the experiments of Arts *et al.* (1990).

Figure 8 shows that, for the high-intensity FVD level $Tu = 6\%$, the boundary-layer disturbances do not exhibit the typical mushroom shape for $\mathcal{G} = 35.2$ and instead resemble the streaks evolving over a flat plate. This occurrence is due to the destabilising effect of the concave wall not being sufficiently intense to alter the character of the disturbances when the FVD level is large. Figures 8(c, f) show that the stabilising effect of the convex wall is also insignificant in the presence of high-intensity FVD as the nonlinear disturbances over convex walls also resemble streaks over a flat plate. This dynamics is in stark contrast with the quiet environment observed in figure 7(c, f) for the convex-wall case at the lower FVD level $Tu = 1\%$.

4.3. Wall-shear stress and wall-heat transfer

Motivated by the dominance of the velocity and temperature modes (0,0) observed in figure 5, we study the streamwise evolution of the skin-friction coefficient and Stanton number, defined as (Anderson 2000)

$$C_f = \frac{2\mu_w}{R_\Lambda} \frac{\partial (U + r_t \hat{u}_{0,0})}{\partial y} \Big|_{y=0}, \quad (4.2)$$

$$S_t = \frac{\kappa_w}{(T_{ad} - T_w) R_\Lambda Pr} \frac{\partial (T + r_t \hat{\tau}_{0,0})}{\partial y} \Big|_{y=0}, \quad (4.3)$$

where μ_w and κ_w are constant because the wall is isothermal.

Another quantity of interest is the Reynolds analogy factor, $R_a = 2S_t/C_f$ (Roy & Blottner 2006), shown in figure 9. It can be utilised to obtain either C_f or S_t when the other quantity is known. Bons (2005) showed that the Reynolds analogy factor depends on the pressure gradient, but it is almost constant for a boundary layer without a pressure gradient. The solid grey line in figure 9 denotes the so-called Chilton–Colburn relation for incompressible laminar boundary layers, namely, $R_a = Pr^{-2/3}$ (Chilton & Colburn 1934), based on experimental data. The Chilton–Colburn value is slightly higher than $R_a = 1.25$, obtained using the Blasius boundary-layer theory. The dashed grey line denotes the value for turbulent boundary layers, reported by Bons (2005). Figure 9 shows that the Reynolds analogy factor for nonlinear Görtler vortices slightly decreases downstream and lies between the laminar and turbulent values. This result is expected since the Görtler vortices develop in a transitional boundary layer. Our computations also show that, as the FVD level increases, the Reynolds analogy factor decreases. This behaviour is opposite to that found by Bons (2005) for turbulent boundary layers.

Figures 10(a, b) show the comparison between our computed skin-friction coefficients and other experimental and numerical data. In figure 10(a), the skin-friction coefficient

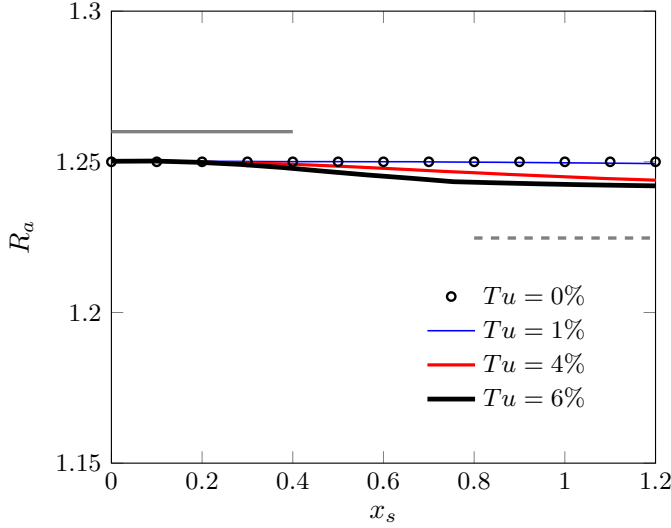


Figure 9: Reynolds analogy factor along the streamwise direction for different FVD levels at $M_\infty = 0.69$. The solid grey line indicates the Reynolds analogy factor for the incompressible laminar flow and the dashed line indicates the experimental measurement of an incompressible turbulent boundary layer by Bons (2005).

is largely unaffected by the FVD level for $Tu \leq 1\%$ and it increases with Tu for $Tu > 1\%$. These results are consistent with the experimental data of Radomsky & Thole (2002). As evidenced in figure 8a of Radomsky & Thole (2002), their measured skin friction on the pressure side of a turbine blade for $Tu = 0.6\%$ is almost the same as that of the laminar flow. Our figure 10(b) shows that their skin-friction coefficient is enhanced by an increase of FVD level. The decrease of skin-friction coefficient with x_s is also in agreement with our result in figure 10(a) as the pressure gradient is not included in our calculations and it is very small in Radomsky & Thole (2002). The main difference is that our skin-friction coefficient becomes almost independent of the streamwise location for $Tu = 6\%$, while their skin-friction coefficient keeps decreasing at all FVD levels, for Tu as large as 19.5%.

Figure 10(b) also shows the experimental data of Arts *et al.* (1990). As the wall-shear stress was not measured by Arts *et al.* (1990), we have used their wall-heat transfer data and computed the skin-friction coefficients via our Reynolds analogy factors. Considering that the Reynolds analogy is not strictly valid in pressure-gradient and transitional flows, our estimate of the skin-friction coefficient can only be regarded as qualitative. Their skin-friction coefficients are enhanced as the FVD level increases, consistently with our results, and grow downstream following the initial decay. This result is markedly different from the decaying trends obtained in our computations and reported by Radomsky & Thole (2002). A reason behind this discrepancy is the difference in geometry of the turbine blades, which leads to different pressure gradients. In the experiments of Radomsky & Thole (2002), the pressure gradient is significantly lower than that of Arts *et al.* (1990), while in our computations the pressure gradient is absent. The direct numerical simulations conducted by Zhao & Sandberg (2020) led to skin-friction coefficients that were independent of the FVD level (refer to their figure 7), a result that remains unexplained.

The wall-heat flux over turbine-blade surfaces is also of interest since experimental measurements have shown its significant enhancement over pressure surfaces (Arts *et al.* 1990; Butler *et al.* 2001). As with the skin-friction coefficient, our computed Stanton numbers are

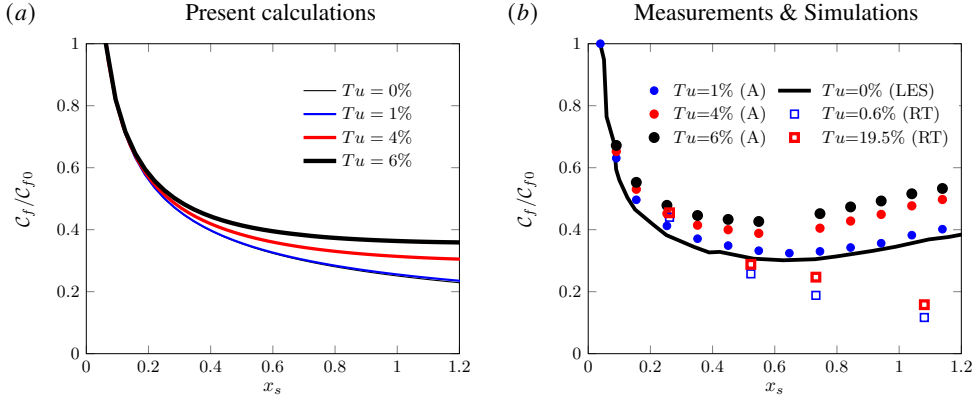


Figure 10: Comparison of (a) the computed skin-friction coefficients with (b) the experimental data of Arts *et al.* (1990) (A) and Radomsky & Thole (2002) (RT). The coefficients are normalised by the value C_{f0} at $x_s = 0.06$. The line in (b) shows the skin-friction coefficient computed by large eddy simulations (LES) without inflow disturbances (Bhaskaran & Lele 2010).

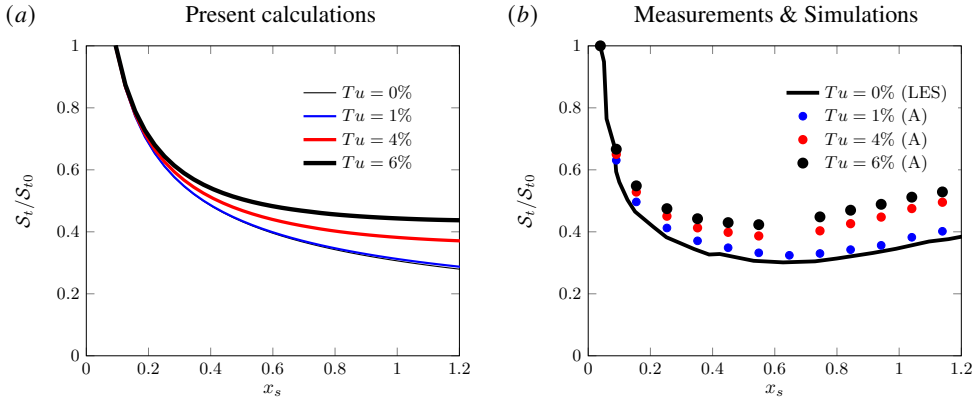


Figure 11: Comparison of (a) the computed Stanton numbers with (b) the experimental data of Arts *et al.* (1990) (A). The Stanton numbers are normalised by the value S_{t0} at $x_s = 0.06$. The line in (b) shows the Stanton number computed by large eddy simulations (LES) without inflow disturbances (Bhaskaran & Lele 2010).

580 unaffected by the change of FVD level up to $Tu = 1\%$ and are enhanced by the FVD level for
 581 $Tu > 1\%$, as reported in figure 11(a). As shown in figure 11(b), the large eddy simulations
 582 of Bhaskaran & Lele (2010) resulted in an intensified laminar wall-heat transfer following
 583 the initial decay, a phenomenon not observed in our computations. As with the skin-friction
 584 coefficient, this discrepancy arises from the absence of streamwise pressure gradient in our
 585 case. Figure 11(b) also depicts the experimental data of Arts *et al.* (1990). Their wall-heat
 586 transfer for $Tu = 1\%$ is only slightly larger than the laminar value and increases with the
 587 FVD level $Tu > 1\%$. Both results agree with our computations and with the response of the
 588 skin friction to a change of FVD level. Ours is the first numerical verification of the effect of
 589 FVD level in the experiments of Arts *et al.* (1990), although the effect of streamwise pressure
 590 gradient needs to be further investigated.

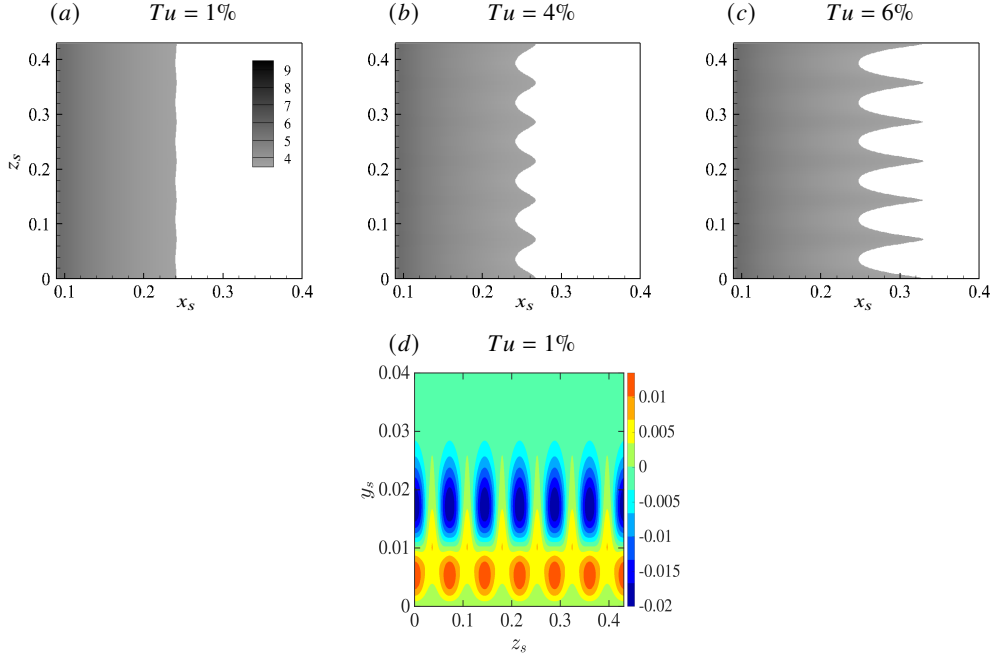


Figure 12: (a – c) Time-averaged wall-shear stress $\mathcal{F}(x_s, z_s)$, defined in equation (4.4), for different FVD levels. Panel (d) shows the contour of the time-averaged streamwise velocity streaks, given by mode (0,2). The wall-normal coordinate is $y_s = y^*/C_{ax}^*$. The Görtler number is $\mathcal{G} = 35.2$.

Figures 12(a – c) show the time-averaged wall-shear stress

$$\mathcal{F}(x_s, z_s) = \mu_w \left. \frac{\partial U}{\partial y} \right|_{y=0} + \mu_w r_t \sum_{n=-\infty}^{\infty} \left. \frac{\partial \hat{u}_{0,n}}{\partial y} \right|_{y=0} e^{ink_z z}, \quad (4.4)$$

where $z_s = z^*/C_{ax}^*$. As the leading edge is approached, $\mathcal{F} \sim \mu_w (F''(0)/T_w) \sqrt{R_\Lambda/(2x)} = 1.70/\sqrt{x_s}$. The region close to the leading edge experiences an intense \mathcal{F} that is almost uniform along the spanwise direction. Further downstream, a distinct streaky structure emerges, characterised by alternating streamwise-elongated low- \mathcal{F} and high- \mathcal{F} regions. These patterns become longer as the FVD level increases from $Tu = 1\%$ to $Tu = 6\%$. They are induced by the steady mode (0,2), as shown in figure 12(d).

Figures 13(a – c) show the time-averaged wall-heat transfer

$$\mathcal{Q}(x_s, z_s) = -\kappa_w \left. \frac{\partial T}{\partial y} \right|_{y=0} - \kappa_w r_t \sum_{n=-\infty}^{\infty} \left. \frac{\partial \hat{\tau}_{0,n}}{\partial y} \right|_{y=0} e^{ink_z z}. \quad (4.5)$$

As the leading edge is approached, $\mathcal{Q} \sim -\kappa_w (T'(0)/T_w) \sqrt{R_\Lambda/(2x)} = -0.41/\sqrt{x_s}$. The spanwise streaky pattern observed in figure 12(a – c) for the wall-shear stress is also detected for the wall-heat flux \mathcal{Q} , although \mathcal{Q} is less affected by the FVD level than \mathcal{F} . Similarly to \mathcal{F} , the wall-heat flux modulation is induced by the steady mode (0,2), as shown in figure 13(d). Our calculations qualitatively reproduce the experimental findings by Butler *et al.* (2001), shown in figure 13(e) and also discussed in Baughn *et al.* (1995). These streaky thermal patterns were obtained by liquid crystals on the pressure side of a turbine blade and have been termed hot fingers. Similarly to our numerical results, the picture in figure

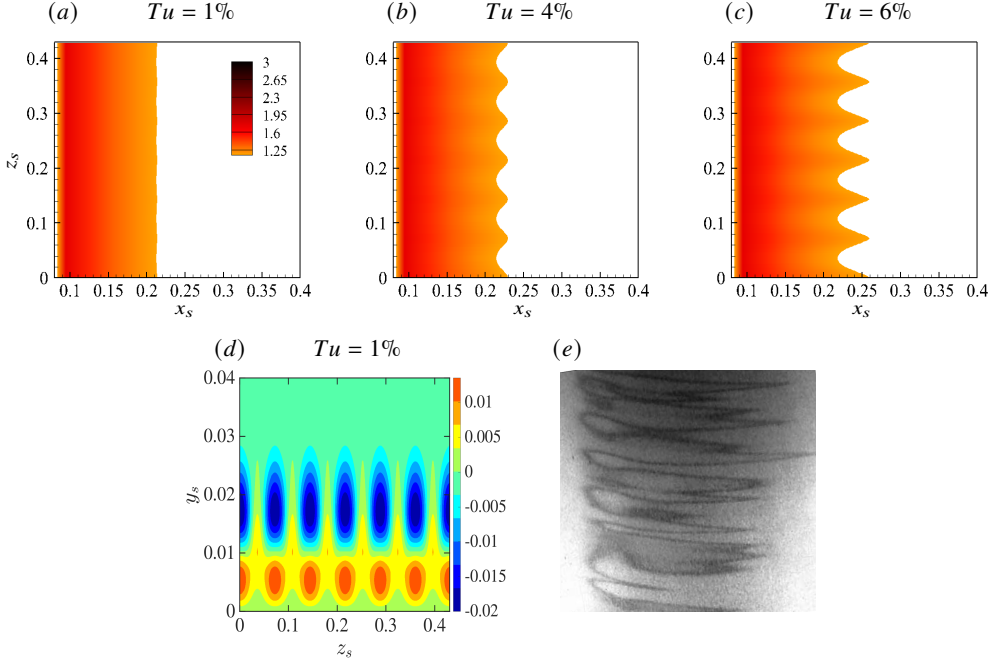


Figure 13: (a – c) Absolute value of the time-averaged wall-heat transfer, $|Q(x_s, z_s)|$, defined in equation (4.5), for different FVD levels. Panel (d) is a contour of the time-averaged temperature streaks, given by mode (0,2). Panel (e) shows the experimental measurements of Butler *et al.* (2001). The Görtler number is $\mathcal{G} = 35.2$.

13(e) shows that the high- Q regions are elongated in the streamwise direction. However, the hot fingers in the experiments display a thin shape upstream before broadening downstream, a feature not observed in our numerical results. This difference could be ascribed to the variation of the streamwise pressure gradient along the blade and to the full spectrum of free-stream turbulence in the experiments, effects that are not included in our computations. Butler *et al.* (2001) and Baughn *et al.* (1995) realised the importance of the FVD intensity on the formation of these patterns, although the occurrence of Görtler vortices was not confirmed.

High-frequency secondary-instability disturbances may influence the trailing edge of the hot fingers, potentially inducing small serrated structures as those depicted in figure 13(e). These smaller structures are, however, less significant than the low-frequency components of the streaks in the formation of the hot fingers and are not computed herein because of our low-frequency assumption. They are discussed in Huang *et al.* (2021) and Feng *et al.* (2024).

Figure 14 illustrates the influence of Mach number on the enhancement of the spanwise modulated patterns of the wall-shear stress and the wall-heat flux. As the Mach number increases at a constant Reynolds number, the skin friction is not affected, while the wall-heat flux is significantly enhanced. We conclude that increasing the turbulence level enhances both the wall-shear stress and the wall-heat transfer, whereas increasing the Mach number only enhances the wall-heat transfer.

4.4. Occurrence map for Görtler vortices and streaks

As discussed in §4.2, both the FVD level and the wall curvature determine whether the boundary-layer disturbances evolve as Görtler vortices or streaks. It is thus useful to discern which type of disturbance occurs under which conditions. We utilise the top graph in figure 15 to this end. It shows the evolution of $u_{rms,max}$ for $\mathcal{G} = 35.2$ and different FVD levels.

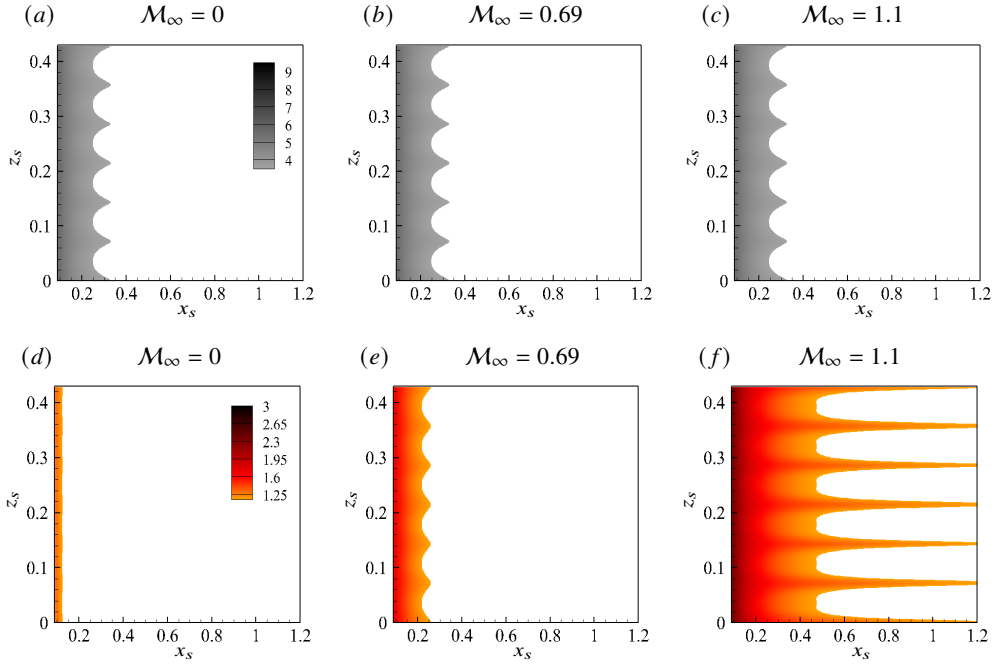


Figure 14: (a – c) Time-averaged wall-shear stress, $\mathcal{F}(x_s, z_s)$, defined in equation (4.4), and (d – f) absolute value of the time-averaged wall-heat transfer, $|\mathcal{Q}(x_s, z_s)|$, defined in equation (4.5). The numerical data are for (a, d) $M_\infty = 0$, (b, e) $M_\infty = 0.69$ and (c, f) $M_\infty = 1.1$.

Linear and nonlinear results are included. The portions of the lines highlighted in red indicate where the evolutions of the boundary-layer disturbances studied by the linear and nonlinear theory overlap. The light red portions of the $u_{rms,max}$ trends grow with a negative concavity, while the dark red portions grow with a positive concavity. The latter do not display a fully exponential growth because nonlinearity quickly sets in leading the disturbance flow to saturation. The dark red portion is clearly visible for $Tu = 0.5\%$, becomes smaller as the FVD level increases to approximately $Tu = 1.8\%$, and disappears for larger Tu as the growth of $u_{rms,max}$ with positive concavity is fully bypassed.

Nonlinear Görtler vortices are defined as boundary-layer disturbances that evolve through three stages from their inception near the leading edge, as shown in the top graph of figure 15, i.e. a light-red growth (such as an algebraic-like $u_{rms,max}$ growth with negative concavity), a dark-red growth (a $u_{rms,max}$ growth with positive concavity) and a saturation stage, where nonlinearity is fully effective and the intensity of the vortices becomes almost independent of the streamwise position. When these flow conditions are met, cross-sectional contour plots of the saturated streamwise velocity and temperature feature the typical mushroom shape, shown in figure 15(a) for $Tu = 0.5\%$. Streaks only exhibit a light-red algebraic-like growth of $u_{rms,max}$ instead of a dark-red growth with positive concavity and feature a bell shape instead of a mushroom shape, shown in figures 15(b, c). They saturate to a nearly constant amplitude, like the nonlinear Görtler vortices.

Using the observations of figure 15, we have created the map shown in figure 16, which identifies the flow character as a function of Tu and \mathcal{G} . The map represents subsonic nonlinearly saturated low-frequency disturbances in boundary layers over concave surfaces. The map is representative of flows over turbine blades with frequencies, Reynolds number and Mach number comparable to the reference values chosen herein. Convex-curvature effects

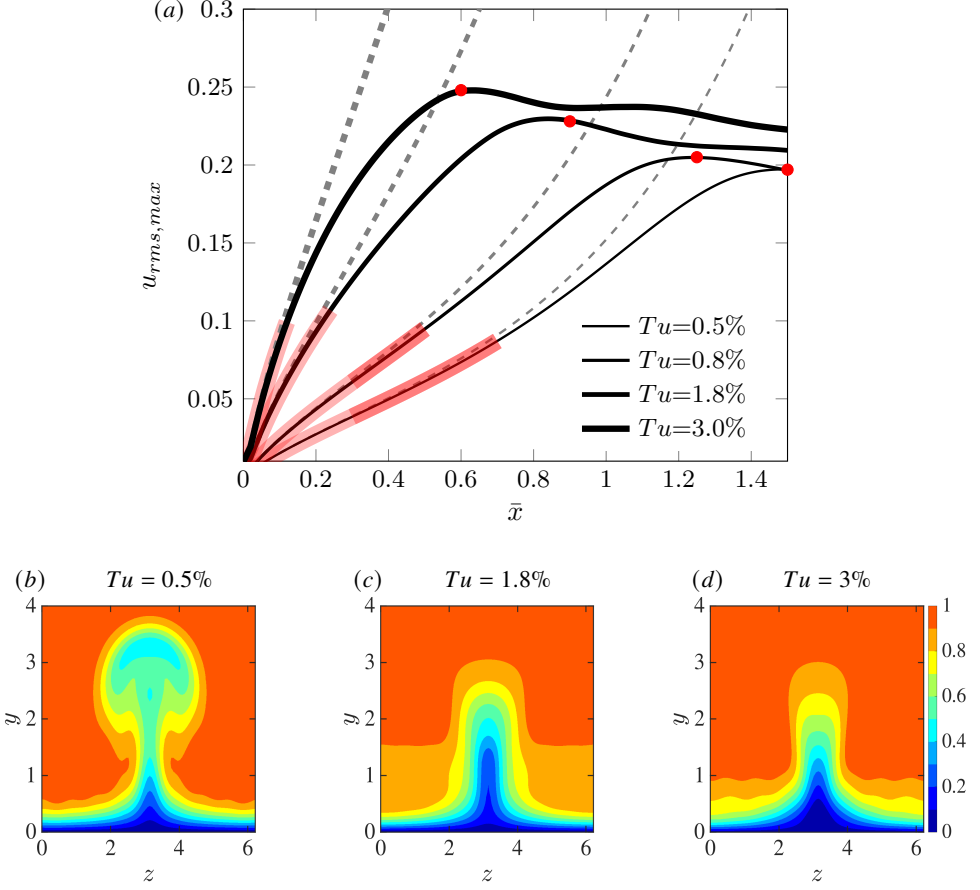


Figure 15: (a) Growth of $u_{rms,max}$ for $\mathcal{G} = 35.2$ and different FVD levels. The portions of the trends highlighted in red indicate where the linear and the nonlinear solutions overlap. The darker portions of the trends denote a $u_{rms,max}$ growth with positive concavity. The saturation points are marked by red circles. Panels (b, c, d) show contours of the instantaneous streamwise velocity $y - z$ plane at the saturation locations for different FVD levels.

are not included as our results indicate that the growth of disturbances is never enhanced with respect to the flat-wall case when the wall is convex.

In the linearised case, for which saturation does not occur, Viaro & Ricco (2018) distinguished Görtler vortices from streaks by applying a criterion solely based on the concavity of the amplitude of the streamwise velocity. This method is, however, inapplicable for nonlinear Görtler vortices because nonlinear disturbances saturate with a null or slightly negative growth rate. If the Viaro–Ricco criterion were applied to the saturated nonlinear disturbances, they would not be classified as Görtler vortices.

As represented in the map of figure 16, Görtler vortices appear when the FVD level is relatively low. The Görtler-vortex region expands as the Görtler number increases. Streaks are instead observed at larger Tu , i.e. when the streamwise curvature is less influential, as discussed in §4.2. As the Görtler number is increased beyond $\mathcal{G} = 100$, the line that separates the two regions flattens to a FVD level slightly below $Tu = 3\%$. This result indicates that, as the Görtler number increases, the wall curvature becomes less influential on whether the nonlinear disturbances evolve as streaks or Görtler vortices. Nonlinear streaks are likely to

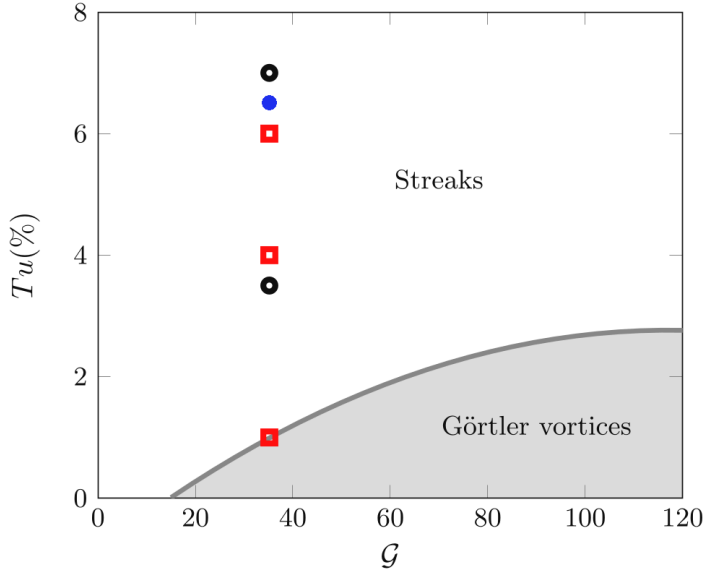


Figure 16: Occurrence map of nonlinear streaks and Görtler vortices for $k_x = 0.0073$, $R_\Lambda = 1124$ and $M_\infty = 0.69$. The symbols denote the data of Zhao & Sandberg (2020) (solid circle), Wheeler *et al.* (2016) (hollow circles) and Arts *et al.* (1990) (hollow squares).

develop over turbine blades because free-stream disturbance environments characterised by $Tu > 3\%$ certainly pertain to turbomachinery flows. Even if boundary layers over turbine blades were exposed to low FVD levels, i.e. $Tu < 3\%$, streaks would still be more likely to occur than Görtler vortices. As discussed in §4.2, the streamwise extent of turbine blades is indeed too limited for the disturbances to be influenced by the wall curvature and turn into Görtler vortices when Tu is low, following the initial algebraic growth highlighted in light red in figure 15. We also note that, while the nonlinear streaks evolving over concave surfaces saturate to a constant amplitude, the nonlinear streaks occurring over flat plates, also termed thermal Klebanoff modes (Marensi *et al.* 2017), typically decay after the initial algebraic growth. The line that distinguishes Görtler vortices from streaks in figure 16 crosses the abscissa at a finite G value, i.e. at any FVD level, small curvatures are not sufficient to trigger Görtler vortices because viscous dissipation overcomes the inviscid centrifugal imbalance (Wu *et al.* 2011; Viaro & Ricco 2018). Furthermore, although FVD are responsible for triggering Görtler vortices and streaks through receptivity, enhancing the FVD level always favours the formation of streaks over Görtler vortices.

In figure 16, experimental and direct numerical simulation data typical of flows over turbine blades and in subsonic wind tunnels are also shown. All those data are located in the ‘streaks’ region, denoting the weak effect of the curvature in boundary layers over the pressure sides of turbine blades. The absence of Görtler vortices over the pressure side of turbine blades was also predicted by Đurović *et al.* (2021), who utilised the criterion by Saric (1994) based on the critical Görtler number. This approach, although successful in their case, is generally not applicable because it is based on three assumptions that are not often satisfied: the Görtler vortices are (i) fully developed along the streamwise direction, which may not be the case because of the limited extent of turbine blades, (ii) described by a linearised dynamics, which is unlikely to be the case for moderate and elevated FVD levels, typical of turbomachinery

applications and (iii) unaffected by non-parallel effects, which instead play a leading role when $\mathcal{G} = O(1)$ (Hall 1983; Wu *et al.* 2011; Xu *et al.* 2017; Marensi & Ricco 2017).

By unravelling the competition between the FVD level and the wall curvature, our occurrence map provides a theoretical explanation for the flow character and instabilities at play in boundary layers over concave walls in the presence of FVD. The map may be used to interpret experiments and simulations of subsonic turbomachinery flows.

4.5. Secondary instability of Görtler vortices and streaks

In this section, we present the results on the secondary instability of the Görtler vortices and streaks. We observe that the dominant fundamental modes are more unstable than the other modes; therefore, we only report the results for the fundamental modes. Figures 17(a, b) display the growth rate ω_i and the phase speed $c_r = \omega_r/\alpha$ of the secondary modes at $\bar{x} = 1.5$ for $Tu = 1\%$, $M_\infty = 0.69$ and $\mathcal{G} = 35.2$. For these conditions, the disturbances are nonlinear Görtler vortices reaching their maximum amplitude. The instability is analysed when the flow is unstable, i.e. in two time windows within a period, from $3\pi/4$ to π and from $7\pi/4$ to 2π . Three dominant unstable modes are detected, one varicose mode (even mode I) and two sinuous modes (odd modes I and II), all of which were shown by Ren & Fu (2015) and Xu *et al.* (2017). At each phase, the maximum growth rate is attained by the even mode I.

Figures 17(c, d) show the growth rate ω_i and the phase speed c_r of the secondary modes at $\bar{x} = 1.5$ for $Tu = 1\%$, $M_\infty = 0.69$ and $\mathcal{G} = 0$. For these conditions, the disturbances are nonlinear streaks since the wall is flat. The growth rate of the odd mode I is relatively low, with a maximum value of about 0.004. Comparing the growth rates in the concave-wall case in figure 17(a) with the growth rate in the flat-wall case in figure 17(c) demonstrates that the curvature significantly increases the growth rate of this secondary-instability mode.

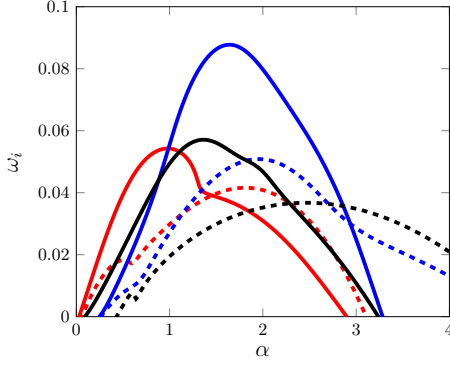
Figures 18(a–c) shows the contours of the streamwise-velocity eigenfunctions of sinuous and varicose modes pertaining to nonlinear Görtler vortices for the same conditions of figures 17(a, b). The eigenfunctions of the unstable odd modes extend across the entire mushroom shape due to the highly distorted velocity profile, while the eigenfunctions of the even modes concentrate at the top of the mushroom shape. Figure 18(d) shows the eigenfunction of the odd mode I pertaining to the nonlinear streaks for the same conditions of figures 17(c, d).

Figure 19 presents the growth rate ω_i and phase speed c_r of secondary modes growing on nonlinear streaks at $\bar{x} = 0.36$ for $Tu = 6\%$. Due to the high FVD level, the growth rate and phase speed are almost the same as those for Görtler vortices, as shown in figure 17. Compared with the Görtler vortices, the time window of instability is shorter, although the dominant mode is still the odd mode I. A new even mode (even mode II) is detected for the nonlinear streaks, which has never been reported in the literature. Both its growth rate and phase speed are smaller than those of the odd mode I. This new mode is not the varicose mode reported in Wu & Choudhari (2003) as the new mode only appears for high-intensity FVD.

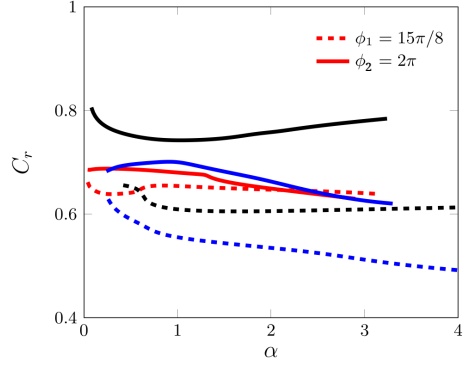
Figure 20 shows the contours of the streamwise-velocity eigenfunctions of the odd mode I and the even mode II for $Tu = 6\%$. The structure of the odd mode I is similar to the odd mode I for the streaks shown in figure 18(d). The even mode II concentrates in the lower part of the streaks and it may thus promote transition to turbulence at the stem of nonlinear streaks.

Our analysis thus suggests that transition to turbulence over the pressure surface of turbine blades subject to high-intensity FVD is due to the breakdown of unsteady nonlinear streaks. We also conclude that transition to turbulence in subsonic wind tunnel can be caused by the breakdown of nonlinear Görtler vortices because of the low-intensity FVD environment and the long streamwise distance along which the vortices can develop.

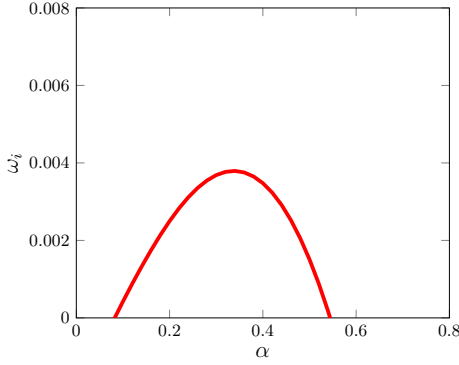
(a)



(b)



(c)



(d)

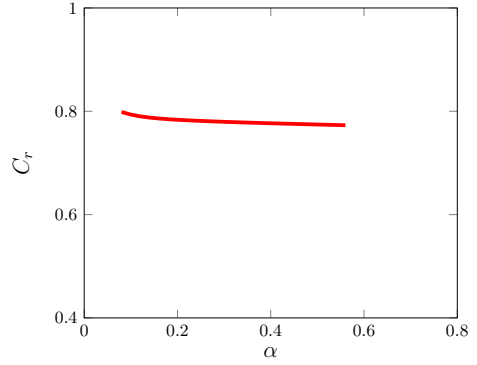


Figure 17: (a, c) Temporal growth rates and (b, d) phase speeds of the secondary-instability modes of Görtler vortices. Panels (a, b) are for the concave-wall case ($\mathcal{G} = 35.2$) and panels (c, d) are for the flat-wall case ($\mathcal{G} = 0$). The red lines represent odd mode I, the blue lines correspond to even mode I and the black lines indicate odd mode II. The parameters are $\bar{x} = 1.5$, $Tu = 1\%$ and $\mathcal{M}_\infty = 0.69$.

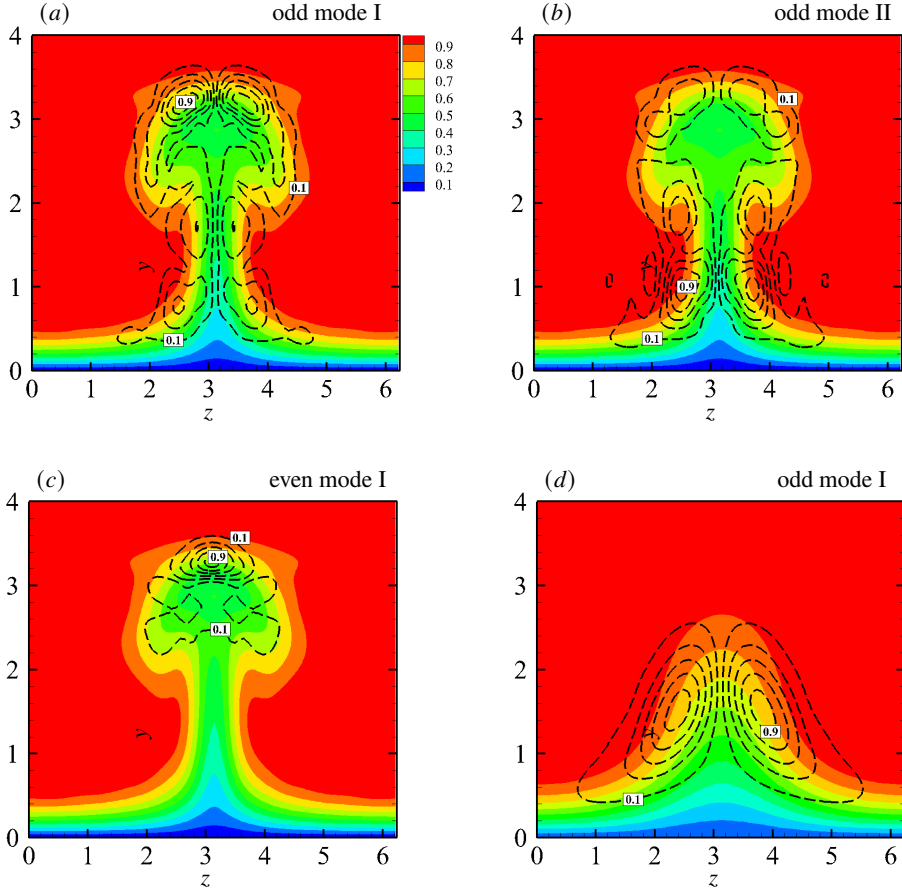


Figure 18: Eigenfunctions of secondary unstable modes, shown by contours of the streamwise velocity (absolute value, black lines). Görtler vortices ($\mathcal{G} = 35.2$): (a) odd mode I; (b) odd mode II; (c) even mode I. Streaks ($\mathcal{G} = 0$): (d) odd mode I. The coloured contours represent the streamwise velocity of the vortex base flow at $\bar{x} = 1.5$. Five levels are specified, ranging from 0.1 to 0.9. The parameters are $Tu = 1\%$ and $M_\infty = 0.69$.

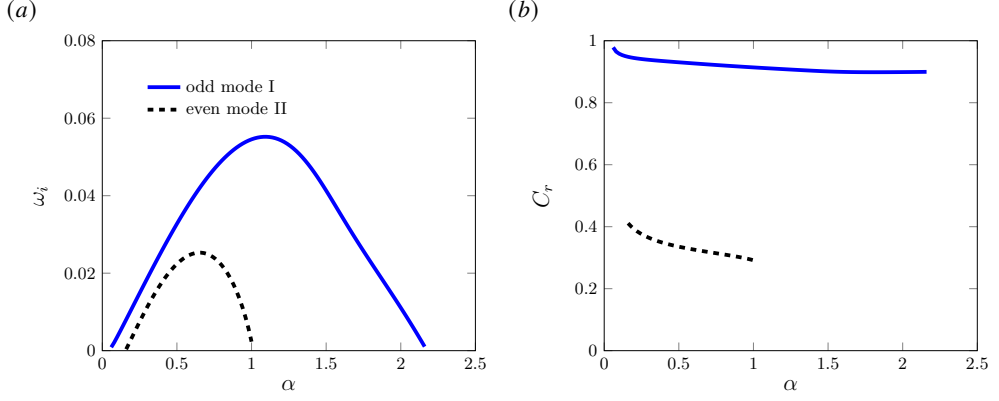


Figure 19: Characteristics of secondary instability of streaks: (a) temporal growth rate and (b) phase speed versus the streamwise wavenumber α . The parameters are $Tu = 6\%$, $\mathcal{G} = 35.2$ and $M_\infty = 0.69$.

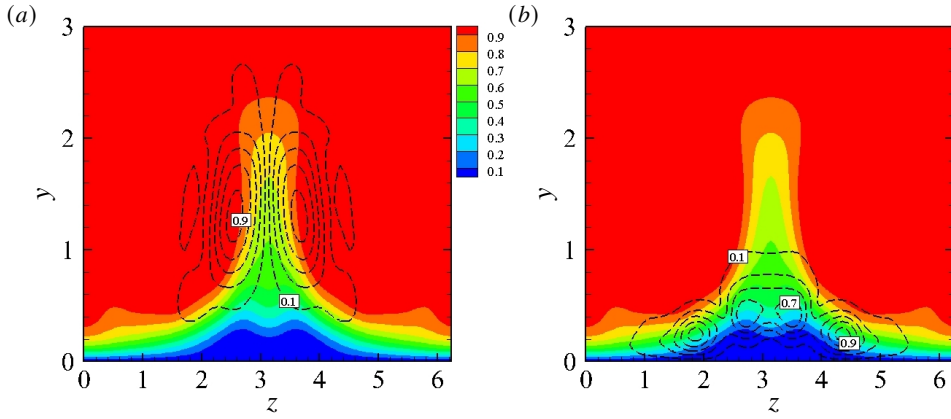


Figure 20: Eigenfunctions (absolute value, black lines) of secondary unstable modes, shown by contours of the streamwise velocity. (a) odd mode I; (b) even mode II. The coloured contours represent the streamwise velocity of the vortex base flow at $\bar{x} = 0.3$. Five levels are specified, ranging from 0.1 to 0.9. The parameters are $Tu = 6\%$, $\mathcal{G} = 35.2$ and $M_\infty = 0.69$.

5. Conclusions

In this study, we have utilised receptivity theory to investigate the nonlinear response of compressible boundary layers over curved surfaces to unsteady free-stream vortical fluctuations of the convected-gust type. We have focused on low-frequency and long-wavelength disturbances because these disturbances penetrate the most into the core of a boundary layer, forming kinematic and thermal Görtler vortices or streaks. The free-stream disturbances are assumed to be strong enough to generate nonlinear interactions between velocity and temperature fluctuations, thus altering the original laminar base flow when the local boundary-layer thickness becomes comparable to the spanwise wavelength of the Görtler vortices or streaks. This boundary-layer response is governed by the compressible boundary-region equations, leading to a nonlinear initial-boundary-value problem that we have solved numerically. Our previous studies by Xu *et al.* (2017), Marensi *et al.* (2017) and Viaro & Ricco (2019a) have been unified to account for compressibility, curvature and nonlinear effects simultaneously.

We have investigated transitional boundary layers for flow parameters pertaining to flows over pressure surfaces of turbine blades. Decreasing the frequency of the free-stream perturbations and increasing the wall concavity and the free-stream disturbance level energise the boundary-layer disturbances. The Mach number instead has no influence on the kinetic disturbances and has a slightly stabilising influence on the thermal disturbances in the subsonic conditions of interest. The disturbances are unsteady along an initial streamwise distance because the unsteadiness of the free-stream flow has a direct impact on the boundary layer. As the flow evolves, steady-flow distortions caused by nonlinearity become comparable to, and may even exceed, the unsteady components induced by the free-stream flow. Our numerical results have been compared with available experimental data for boundary-layer flows over curved pressure surfaces of turbine blades. The receptivity framework accurately predicts the streamwise-elongated spanwise patterns of enhanced skin friction and wall-heat transfer, often referred to as hot fingers.

We have also created a map that identifies the occurrence of saturated nonlinear Görtler vortices and streaks, for different Görtler numbers and free-stream disturbance levels. Nonlinear streaks are defined as disturbances that only grow algebraically and exhibit a bell-like shape. The streaks are more likely to occur at small Görtler numbers and at relatively high levels of ambient disturbances; for high Görtler numbers, a free-stream disturbance level slightly exceeding 3% generates streaks only. Nonlinear Görtler vortices are instead defined as disturbances that display a growth with positive curvature following an initial algebraic growth and feature a mushroom-like shape. The Görtler vortices occur at low levels of free-stream disturbance and intensify as the Görtler number increases.

We have studied the secondary instability of the nonlinear boundary-layer disturbances to elucidate the subsequent stages of the transition process. Our numerical results indicate that the saturated disturbances are susceptible to exponentially growing high-frequency modes. Increasing the streamwise curvature promotes the growth of two odd modes and one even mode. Görtler vortices and streaks excited by high-intensity free-stream disturbances are susceptible to a new even mode (even mode II), which has not been reported in earlier studies. This mode is important since it is located at the stem of the streaks and may thus initiate transition to turbulence there. The even mode II could potentially be more critical than the more unstable odd mode I because its concentration near the wall may cause the resulting transition to affect the skin friction and the wall-heat transfer immediately. In contrast, the odd mode I, located in the outer part of the boundary layer, will not substantially influence the skin friction and the wall-heat transfer until transition extends to the wall.

To conclude, the present study has provided a mathematical and numerical description of the generation, evolution and secondary instability of Görtler vortices and streaks in

compressible boundary layers. The central result is that, thanks to the receptivity approach, the characteristics of the free-stream disturbance environment have been linked quantitatively to the transitional boundary layer. Our analysis can be readily extended to more realistic cases, including boundary layers exposed to broadband free-stream turbulence (Zhang *et al.* 2011) or influenced by a streamwise pressure gradient (Xu *et al.* 2020).

An important avenue of future research is the study of amplified three-dimensional waves developing on the streaks, as recently observed in hypersonic boundary-layer flows by Huang *et al.* (2021) and Feng *et al.* (2024), and previously studied in incompressible boundary layers by Lee & Wu (2008), Jiang *et al.* (2020a), Jiang *et al.* (2020b) and Jiang *et al.* (2021). As shown by Huang *et al.* (2021) and Feng *et al.* (2024), these three-dimensional waves feature overlapped temperature peaks and high-frequency modes, and play an important role in the breakdown to turbulence. In our future work, we plan to focus on the final stages of transition to turbulence and, therefore, it would be interesting to investigate how free-stream perturbations and wall curvature influence the formation of these three-dimensional waves.

For an accurate prediction of the transition location in boundary layers over turbine blades, the leading-edge bluntness should also be taken into account. Transition prediction methods would thus be possible for turbomachinery flows and other compressible flows of industrial interest.

Acknowledgments

We thank the reviewers for their helpful comments that have helped improve the quality of the paper. DX would like to thank Professor Ming Dong, Dr Runjie Song and Dr Lei Zhao for the useful discussions. DR and PR wish to acknowledge the support of EPSRC (Grant No. EP/T01167X/1). PR has also been supported by the US Air Force through the AFOSR grant FA8655-21-1-7008 (International Program Office Dr Douglas Smith).

Declaration of Interests

The authors report no conflict of interest.

Appendix A. Initial conditions for the boundary-region equations

The initial conditions are derived by first seeking a power series solution of the boundary-region equations for $\bar{x} \ll 1$ and $\eta = O(1)$

$$\{\bar{u}, \bar{v}, \bar{w}, \bar{\tau}, \bar{p}\} = \sum_{j=0}^{\infty} (2\bar{x})^{j/2} \left\{ 2\bar{x}U_j(\eta), \sqrt{2\bar{x}}V_j(\eta), k_z^{-1}W_j(\eta), 2\bar{x}T_j(\eta), P_j(\eta)/\sqrt{2\bar{x}} \right\},$$

and by constructing a composite solution that is valid for all values of η . This procedure yields the initial conditions

$$\bar{x} \rightarrow 0] \quad \hat{u}_{1,\pm 1} \rightarrow q_{\pm} \left(2\bar{x}U_0 + (2\bar{x})^{3/2}U_1 \right), \quad (\text{A } 1)$$

$$\begin{aligned} \hat{v}_{1,\pm 1} \rightarrow q_{\pm} \left[V_0 + (2\bar{x})^{1/2}V_1 - \left(V_c - \frac{1}{2}g_1|\kappa_z|(2\bar{x})^{1/2} \right) e^{-|\kappa_z|(2\bar{x})^{1/2}\bar{\eta}} \right. \\ \left. + \frac{i}{(\kappa_y - i|\kappa_z|)(2\bar{x})^{1/2}} \left(e^{i\kappa_y(2\bar{x})^{1/2}\bar{\eta} - (\kappa_z^2 + \kappa_y^2)\bar{x}} - e^{-|\kappa_z|(2\bar{x})^{1/2}\bar{\eta}} \right) - \bar{v}_c \right], \end{aligned} \quad (\text{A } 2)$$

$$\begin{aligned} \hat{w}_{1,\pm 1} \rightarrow \mp i q_{\pm} \left[W_0 + (2\bar{x})^{1/2}W_1 - V_c|\kappa_z|(2\bar{x})^{1/2}e^{-|\kappa_z|(2\bar{x})^{1/2}\bar{\eta}} \right. \\ \left. + \frac{1}{\kappa_y - i|\kappa_z|} \left(\kappa_y e^{i\kappa_y(2\bar{x})^{1/2}\bar{\eta} - (\kappa_z^2 + \kappa_y^2)\bar{x}} - i|\kappa_z|e^{-|\kappa_z|(2\bar{x})^{1/2}\bar{\eta}} \right) - \bar{w}_c \right], \end{aligned} \quad (\text{A } 3)$$

$$\hat{p}_{1,\pm 1} \rightarrow q_{\pm} \left[\frac{P_0}{(2\bar{x})^{1/2}} + P_1 + \left(g_1 - \frac{V_c}{|\kappa_z|(2\bar{x})^{1/2}} \right) e^{-|\kappa_z|(2\bar{x})^{1/2}\bar{\eta}} - \bar{p}_c \right], \quad (\text{A } 4)$$

$$\bar{\tau}_{1,\pm 1} \rightarrow q_{\pm} \left(2\bar{x}T_0 + (2\bar{x})^{3/2}T_1 \right), \quad (\text{A } 5)$$

where $\bar{\eta} \equiv \eta - \beta_c$ and $\beta_c = \lim_{\eta \rightarrow \infty} (\eta - F)$. The common parts \bar{v}_c , \bar{w}_c and \bar{p}_c , the constants g_1 and V_c and the solutions $U_0, V_0, W_0, P_0, T_0, U_1, V_1, W_1, P_1, T_1$ are given in Appendix D of Ricco (2007). The term q_{\pm} herein represents the amplitude of the induced disturbances. In the case of a pair of oblique modes, it is given by

$$q_{\pm} = \pm \frac{i\kappa_z^2}{k_z} \left(\hat{u}_{z,\pm}^{\infty} \pm \frac{ik_z}{\sqrt{k_x^2 + k_z^2}} \hat{u}_{y,\pm}^{\infty} \right).$$

REFERENCES

- ANDERSON, J. D. 2000 *Hypersonic and high temperature gas dynamics*. AIAA-Education Series-2nd edition.
- ARTS, T., LAMBERTDEROUVOIT, M. & RUTHERFORD, A. W. 1990 Aero-thermal investigation of a highly loaded transonic linear turbine guide vane cascade. A test case for inviscid and viscous flow computations. Technical Note 174. van Kármán Institute.
- BAUGHN, J. W., BUTLER, R. J., BYERLEY, A. R. & RIVIR, R. B. 1995 An experimental investigation of heat transfer, transition and separation on turbine blades at low Reynolds number and high turbulence intensity. *ASME Paper* 95-WA/HT-25.
- BECKWITH, I. E., HARVEY, W. D., HARRIS, J. E. & HOLLEY, B. B. 1973 Control of supersonic wind-tunnel noise by laminarization of nozzle-wall boundary layers. NASA TM X-2879. NASA Langley Research Center.
- BHASKARAN, R. & LELE, S. K. 2010 Large eddy simulation of free-stream turbulence effects on heat transfer to a high-pressure turbine cascade. *J. Turbul.* (11), N6.
- BOGOLEPOV, V. V. 2001 Asymptotic analysis of the structure of long-wave Görtler vortices in a hypersonic boundary layer. *J. Appl. Mech. Tech. Phys.* **42** (5), 773–785.
- BONS, J. 2005 A critical assessment of Reynolds analogy for turbine flows. *J. Heat Transfer* **127** (5), 472–485.
- BUTLER, R. J., BYERLEY, A. R., VANTREUREN, K. & BAUGHN, J. W. 2001 The effect of turbulence intensity and length scale on low-pressure turbine blade aerodynamics. *Int. J. Heat Fluid Flow* **22** (2), 123–133.
- CAMCI, C. & ARTS, T. 1990 An experimental convective heat transfer investigation around a film-cooled gas turbine blade. *J. Turbom.* **112** (3), 497–503.
- CANUTO, C., HUSSAINI, M. Y., QUARTERONI, A. & ZANG, T. A. 1988 *Spectral methods in fluid dynamics*. New York: Springer-Verlag.

- CHILTON, T. H. & COLBURN, A. P. 1934 Mass transfer (absorption) coefficients prediction from data on heat transfer and fluid friction. *Ind. Engng Chem.* **26** (11), 1183–1187.
- DANDO, A. H. & SEDDOUGUI, S. O. 1993 The compressible Görtler problem in two-dimensional boundary layers. *IMA J. Appl. Math.* **51** (1), 27–67.
- FENG, Z., CAI, C., LEE, C. & YANG, D. 2024 Investigation of an overlap of heating peaks in the hypersonic boundary layer over a blunt cone. *Phys. Rev. Fluids* **9** (7), L071901.
- FLORYAN, J. M. 1991 On the Görtler instability of boundary layers. *Prog. Aerosp. Sci.* **28** (3), 235–271.
- FRANSSON, J.H.M. & SHAHINFAR, S. 2020 On the effect of free-stream turbulence on boundary-layer transition. *J. Fluid Mech.* **899**, A23.
- FU, Y. & HALL, P. 1991a Effects of Görtler vortices, wall cooling and gas dissociation on the Rayleigh instability in a hypersonic boundary layer. NASA Rep. 91-87.
- FU, Y. & HALL, P. 1991b Nonlinear development and secondary instability of Görtler vortices in hypersonic flows. NASA Rep. 91-39.
- GHOORBANIAN, K., SOLTANI, M. R. & MANSHADI, M. D. 2011 Experimental investigation on turbulence intensity reduction in subsonic wind tunnels. *Aerosp. Sci. Technol.* **15** (2), 137–147.
- GOURDAIN, N., GICQUEL, L. Y. M. & COLLADO, E. 2012 Comparison of RANS and LES for prediction of wall heat transfer in a highly loaded turbine guide vane. *J. Propuls. Power* **28** (2), 423–433.
- HALL, P. 1982 Taylor—görtler vortices in fully developed or boundary-layer flows: linear theory. *J. Fluid Mech.* **124**, 475 – 494.
- HALL, P. 1983 The linear development of Görtler vortices in growing boundary layers. *J. Fluid Mech.* **130** (41), 243–266.
- HALL, P. 1990 Görtler vortices in growing boundary layers: the leading edge receptivity problem, linear growth and the nonlinear breakdown stage. *Mathematika* **37** (74), 151–189.
- HALL, P. & FU, Y. 1989 On the Görtler vortex instability mechanism at hypersonic speeds. *Theor. Comput. Fluid Dyn.* **1** (3), 125–134.
- HALL, P. & MALIK, M. 1989 The growth of Görtler vortices in compressible boundary layers. *J. Eng. Math.* **23** (3), 239–251.
- HUANG, G., SI, W. & LEE, C. 2021 Inner structures of Görtler streaks. *Phys. Fluids* **33** (3), 034116.
- JIANG, X. Y., GU, D. W., LEE, C. B., SMITH, C. R. & LINDEN, P. F. 2021 A metamorphosis of three-dimensional wave structure in transitional and turbulent boundary layers. *J. Fluid Mech.* **914**, A4.
- JIANG, X. Y., LEE, C. B., CHEN, X., SMITH, C. R. & LINDEN, P. F. 2020a Structure evolution at early stage of boundary-layer transition: simulation and experiment. *J. Fluid Mech.* **890**, A11.
- JIANG, X. Y., LEE, C. B., SMITH, C. R., CHEN, J. W. & LINDEN, P. F. 2020b Experimental study on low-speed streaks in a turbulent boundary layer at low Reynolds number. *J. Fluid Mech.* **903**, A6.
- KANANI, Y., ACHARYA, S. & AMES, F. 2019 Large eddy simulation of the laminar heat transfer augmentation on the pressure side of a turbine vane under freestream turbulence. *ASME J. Turbomach.* **141** (4), 041004.
- LEE, C. B. & WU, J. Z. 2008 Transition in wall-bounded flows. *Appl. Mech. Rev.* **61** (3), 030802.
- LEIB, S. J., WUNDROW, D. W. & GOLDSTEIN, M. E. 1999 Effect of free-stream turbulence and other vortical disturbances on a laminar boundary layer. *J. Fluid Mech.* **380**, 169–203.
- LENGANI, D., SIMONI, D., PRALITS, J. O., ĐUROVIĆ, K., DE VINCENTIIS, L., HENNINGSON, D. S. & HANIFI, A. 2022 On the receptivity of low-pressure turbine blades to external disturbances. *J. Fluid Mech.* **937**, A36.
- MARENSI, E. & RICCO, P. 2017 Growth and wall-transpiration control of nonlinear unsteady Görtler vortices forced by free-stream vortical disturbances. *Phys. Fluids* **29** (11), 114106.
- MARENSI, E., RICCO, P. & WU, X. 2017 Nonlinear unsteady streaks engendered by the interaction of free-stream vorticity with a compressible boundary layer. *J. Fluid Mech.* **817**, 80–121.
- MATSUBARA, M. & ALFREDSSON, P.H. 2001 Disturbance growth in boundary layers subjected to free-stream turbulence. *J. Fluid Mech.* **430**, 149–168.
- MAYLE, R. E. 1991 The 1991 IGTI scholar lecture: the role of laminar-turbulent transition in gas turbine engines. *Trans. ASME J. Turbomach.* **113**, 509–537.
- MORATA, E. C., GOURDAIN, N., DUCHAINE, F. & GICQUEL, L. Y. M. 2012 Effects of free-stream turbulence on high pressure turbine blade heat transfer predicted by structured and unstructured LES. *Int. J. Heat Mass Transf.* **55** (21-22), 5754–5768.
- NAGARAJAN, S., LELE, S. K. & FERZIGER, J. H. 2007 Leading-edge effects in bypass transition. *J. Fluid Mech.* **572**, 471–504.

- 911 QIN, F. & WU, X. 2016 Response and receptivity of the hypersonic boundary layer past a wedge to free-stream
912 acoustic, vortical and entropy disturbances. *J. Fluid Mech.* **797**, 874–915.
- 913 RADOMSKY, R. W. & THOLE, K. A. 2002 Detailed boundary layer measurements on a turbine stator vane at
914 elevated freestream turbulence levels. *ASME J. Turbomach.* **124** (1), 107–118.
- 915 REN, J. & FU, S. 2014 Competition of the multiple Görtler modes in hypersonic boundary layer flows. *Sci.*
916 *China Phys. Mech. Astron.* **57** (6), 1178–1193.
- 917 REN, J. & FU, S. 2015 Secondary instabilities of Görtler vortices in high-speed boundary layer flows. *J. Fluid*
918 *Mech.* **781**, 388–421.
- 919 RICCO, P. 2007 Response of a compressible laminar boundary layer to free-stream turbulent disturbances.
920 PhD thesis, Imperial College London (University of London).
- 921 RICCO, P., LUO, J. & WU, X. 2011 Evolution and instability of unsteady nonlinear streaks generated by free-
922 stream vortical disturbances. *J. Fluid Mech.* **677**, 1–38.
- 923 RICCO, P. & WU, X. 2007 Response of a compressible laminar boundary layer to free-stream vortical
924 disturbances. *J. Fluid Mech.* **587**, 97–138.
- 925 ROY, C. J. & BLOTTNER, F. G. 2006 Review and assessment of turbulence models for hypersonic flows. *Prog.*
926 *Aerosp. Sci.* **42** (7–8), 469–530.
- 927 SARIC, W. S. 1994 Görtler vortices. *Annu. Rev. Fluid Mech.* **26** (1), 379–409.
- 928 SCHNEIDER, S. P. 1999 Flight data for boundary-layer transition at hypersonic and supersonic speeds. *J.*
929 *Spacecr. Rockets* **36** (1), 8–20.
- 930 SCHNEIDER, S. P. 2008 Development of hypersonic quiet tunnels. *J. Space. Rock.* **45-4**, 641–664.
- 931 SCHNEIDER, S. P. 2015 Developing mechanism-based methods for estimating hypersonic boundary-layer
932 transition in flight: The role of quiet tunnels. *Progr. Aerosp. Sc.* **72**, 17–29.
- 933 SCHULTZ, M. P. & VOLINO, R. J. 2003 Effects of concave curvature on boundary layer transition under high
934 freestream turbulence conditions. *J. Fluids Eng.* **125** (1), 18–27.
- 935 SESCO, A., AFSAR, M. & HATTORI, Y. 2020 Streaks in high-speed boundary layers: a view through the full
936 nonlinear boundary-region equations. *AIAA Paper* 2020-0830.
- 937 SONG, R., ZHAO, L. & HUANG, Z. 2020 Secondary instability of stationary Görtler vortices originating from
938 first/second Mack mode. *Phys. Fluids* **32** (3).
- 939 STEWARTSON, K. 1964 *The theory of laminar boundary layers in compressible fluids*. Clarendon Press
940 Oxford.
- 941 SUN, Y. & SMITH, H. 2017 Review and prospect of supersonic business jet design. *Prog. Aerosp. Sci.* **90**,
942 12–38.
- 943 ĐUROVIĆ, K., DE VINCENTIIS, L., SIMONI, D., LENGANI, D., PRALITS, J., HENNINGSON, D. S. & HANIFI, A.
944 2021 Free-stream turbulence-induced boundary-layer transition in low-pressure turbines. *ASME J.*
945 *Turbomach.* **143** (8), 081015.
- 946 VARTY, J. W. & AMES, F. E. 2016 Experimental heat transfer distributions over an aft loaded vane with a large
947 leading edge at very high turbulence levels. *ASME Paper* IMECE2016-67029.
- 948 VIARO, S. & RICCO, P. 2018 Neutral stability curves of low-frequency Görtler flow generated by free-stream
949 vortical disturbances. *J. Fluid Mech.* **845**, R1.
- 950 VIARO, S. & RICCO, P. 2019a Compressible unsteady Görtler vortices subject to free-stream vortical
951 disturbances. *J. Fluid Mech.* **867**, 250–299.
- 952 VIARO, S. & RICCO, P. 2019b Neutral stability curves of compressible Görtler flow generated by low-frequency
953 free-stream vortical disturbances. *J. Fluid Mech.* **876**, 1146–1157.
- 954 WHEELER, A. P. S., SANDBERG, R. D., SANDHAM, N. D., PICHLER, R., MICHELASSI, V. & LASKOWSKI, G. 2016
955 Direct numerical simulations of a high-pressure turbine vane. *ASME J. Turbomach.* **138** (7).
- 956 WRIGHT, L. M., MALAK, M. F., CRITES, D. C., MORRIS, M. C., YELAVKAR, V. & BILWANI, R. 2014 Review of
957 platform cooling technology for high pressure turbine blades. *ASME Paper* GT2014-26373.
- 958 WU, X. & CHOUDHARI, M. 2003 Linear and nonlinear instabilities of a blasius boundary layer perturbed by
959 streamwise vortices. Part 2. intermittent instability induced by long-wavelength Klebanoff modes. *J.*
960 *Fluid Mech.* **483**, 249–286.
- 961 WU, X., ZHAO, D. & LUO, J. 2011 Excitation of steady and unsteady Görtler vortices by free-stream vortical
962 disturbances. *J. Fluid Mech.* **682**, 66–100.
- 963 XU, D., LIU, J. & WU, X. 2020 Görtler vortices and streaks in boundary layer subject to pressure gradient:
964 excitation by free stream vortical disturbances, nonlinear evolution and secondary instability. *J. Fluid*
965 *Mech.* **900**, A15.
- 966 XU, D., RICCO, P. & DUAN, L. 2024 Görtler instability and transition in compressible flows. *AIAA J.* **62** (2),
967 489–517.

- 968 XU, D., ZHANG, Y. & WU, X. 2017 Nonlinear evolution and secondary instability of steady and unsteady
969 Görtler vortices induced by free-stream vortical disturbances. *J. Fluid Mech.* **829**, 681–730.
- 970 ZHANG, Y., ZAKI, T., SHERWIN, S. & WU, X. 2011 Nonlinear response of a laminar boundary layer to isotropic
971 and spanwise localized free-stream turbulence. *AIAA Paper* 2011-3292.
- 972 ZHAO, Y. & SANDBERG, R. D. 2020 Bypass transition in boundary layers subject to strong pressure gradient
973 and curvature effects. *J. Fluid Mech.* **888**, A4.